# scientific reports



### **OPEN**

# Diastolic dysfunction in Alzheimer's disease model mice is associated with A\beta-amyloid aggregate formation and mitochondrial dysfunction

Richa Aishwarya<sup>1</sup>, Chowdhury S. Abdullah<sup>1</sup>, Naznin Sultana Remex<sup>2</sup>, Mohammad Alfrad Nobel Bhuiyan<sup>3</sup>, Xiao-Hong Lu<sup>4</sup>, Nirav Dhanesha<sup>1</sup>, Karen Y. Stokes<sup>2</sup>, A. Wayne Orr<sup>1,2</sup>, Christopher G. Kevil<sup>1,2</sup> & Md. Shenuarin Bhuiyan<sup>1,2⊠</sup>

Alzheimer's Disease (AD) is a progressive neurodegenerative disease caused by the deposition of Aβ aggregates or neurofibrillary tangles. AD patients are primarily diagnosed with the concurrent development of several cardiovascular dysfunctions. While few studies have indicated the presence of intramyocardial Aß aggregates, none of the studies have performed detailed analyses for pathomechanism of cardiac dysfunction in AD patients. This manuscript used aged APPSWE/PS1Tq and littermate age-matched wildtype (Wt) mice to characterize cardiac dysfunction and analyze associated pathophysiology. Detailed assessment of cardiac functional parameters demonstrated the development of diastolic dysfunction in APPSWE/PS1Tg hearts compared to Wt hearts. Muscle function evaluation showed functional impairment (decreased exercise tolerance and muscle strength) in APP<sup>SWE</sup>/PS1 Tq mice. Biochemical and histochemical analysis revealed A $\beta$  aggregate accumulation in APPSWE/PS1Tg mice myocardium. APPSWE/PS1Tg mice hearts also demonstrated histopathological remodeling (increased collagen deposition and myocyte cross-sectional area). Additionally, APPSWE/ PS1Tg hearts showed altered mitochondrial dynamics, reduced antioxidant protein levels, and impaired mitochondrial proteostasis compared to Wt mice. APPSVE/PS1Tq hearts also developed mitochondrial dysfunction with decreased OXPHOS and PDH protein complex expressions, altered ETC complex dynamics, decreased complex activities, and reduced mitochondrial respiration. Our results indicated that Aß aggregates in APPSWE/PS1Tg hearts are associated with defects in mitochondrial respiration and complex activities, which may collectively lead to cardiac diastolic dysfunction and myocardial pathological remodeling.

Keywords Diastolic dysfunction, Alzheimer's disease, Fibrosis, Mitochondrial dysfunction

Alzheimer's Disease (AD) is a progressive neurodegenerative disease characterized by loss of memory, confusion, poor judgment, apathy, depression, and difficulty in walking and speaking<sup>1</sup>. AD is primarily caused by the deposition of  $\beta$ -amyloid (A $\beta$ ), tau protein aggregates, and neurofibrillary tangles (NFTs). Several hypotheses explain AD pathophysiology, including cholinergic, amyloid, tau propagation, mitochondrial cascade, calcium homeostasis and NMDA, neurovascular, inflammatory, metal ion, and lymphatic system<sup>2,3</sup>. Among all these hypotheses, the amyloid hypothesis provides a mechanistic understanding of AD<sup>2,4</sup> and focuses on A $\beta$  aggregate formation as AD's main player and initiator. A $\beta$  aggregates are formed by the cleavage of Amyloid Precursor Protein (APP), which is cleaved by  $\alpha$ , or  $\beta$  and  $\gamma$  secretase enzymes forming soluble or insoluble protein fragments.

<sup>1</sup>Department of Pathology and Translational Pathobiology, Louisiana State University Health Sciences Center-Shreveport, Shreveport, LA 71130, USA. <sup>2</sup>Department of Molecular and Cellular Physiology, Louisiana State University Health Sciences Center-Shreveport, Shreveport, LA 71103, USA. <sup>3</sup>Department of Medicine, Division of Clinical Informatics, Louisiana State University Health Sciences Center-Shreveport, Shreveport, LA 71103, USA. <sup>4</sup>Department of Pharmacology, Toxicology and Neuroscience, Louisiana State University Health Sciences Center-Shreveport, Shreveport, LA 71103, USA. <sup>5</sup>Department of Pharmacology, Toxicology and Neuroscience, Louisiana State University Health Sciences Center-Shreveport, Shreveport, LA 71103, USA. <sup>5</sup>Department of Pharmacology, Toxicology and Neuroscience, Louisiana State University Health Sciences Center-Shreveport, Shreveport, LA 71103, USA. <sup>5</sup>Department of Pharmacology, Toxicology and Neuroscience, Louisiana State University Health Sciences Center-Shreveport, Shreveport, LA 71103, USA. <sup>5</sup>Department of Pharmacology, Toxicology and Neuroscience, Louisiana State University Health Sciences Center-Shreveport, Shreveport, LA 71103, USA. <sup>5</sup>Department of Pharmacology, Toxicology and Neuroscience, Louisiana State University Health Sciences Center-Shreveport, LA 71103, USA. <sup>5</sup>Department of Pharmacology, Toxicology and Neuroscience, Louisiana State University Health Sciences Center-Shreveport, LA 71103, USA. <sup>5</sup>Department of Pharmacology, Toxicology and Neuroscience, Louisiana State University Health Sciences Center-Shreveport, LA 71103, USA. <sup>5</sup>Department of Pharmacology, Toxicology and Neuroscience, Louisiana State University Health Sciences Center-Shreveport, LA 71103, USA. <sup>5</sup>Department of Pharmacology, Toxicology and Neuroscience, Louisiana State University Health Sciences Center-Shreveport, LA 71103, USA. <sup>5</sup>Department of Pharmacology, Toxicology and Neuroscience, Louisiana State University Health Sciences Center-Shreveport, LA 71103, USA. <sup>5</sup>Department of Pharmacology and Pharm

Sequential cleavage of APP by  $\alpha$  and  $\gamma$  secretases leads to the formation of soluble sAPP $\alpha$  (normal processing) whereas, sequential cleavage of APP by  $\beta$  ( $\beta$ -site APP-cleaving enzyme 1 (BACE1)) and  $\gamma$  secretases (complex of presenilin 1 (PSEN1) or PSEN2, nicastrin, presenilin enhancer 2, and anterior pharynx-defective 1) leads to the formation of APP $\beta$  ( $A\beta$ ), i.e., sticky  $A\beta$  peptides that aggregate to form oligomers which then further aggregates to form amyloid fibrils<sup>3,5,6</sup>. Another well-accepted mechanism for AD is the deposition of NFTs consisting of hyper-phosphorylated tau protein<sup>6,7</sup>. Hyper-phosphorylated tau forms paired helical filaments (PHFs), which then aggregate to form NFTs<sup>2,3,6,8</sup>. Aggregation of  $A\beta$  and NFTs causes neuronal loss, leading to cognitive impairment<sup>2,3,6,8,9</sup>. Previous studies have revealed the presence of several mutations in the APP gene, altered APP processing resulting in toxic and aggregation-prone  $A\beta$  species accumulation, or hyperphosphorylated tau protein(i.e. microtubule associate protein tau (MAPT) gene) in AD patients<sup>3</sup>.

Based on the mutations present in AD patients, several preclinical models have been established to understand the pathophysiology of AD using vertebrate animals, including mice, rats, non-human primates, dogs, and guinea pigs, invertebrate animals including *Drosophila*, *C. elegans*, and lower order animals including zebrafish<sup>10</sup>. Several mice models with different mutations including PDAPP, Tg2576, APP23, J20, TgCRND8, PS2APP, APP<sup>SWE</sup>/PSEN1dE9, Tg-ArcSwe, 5xFAD, 6xFAD, A7, NL-G-F, 3xTg, JNPL3, PS19, rTg4510, MAPT knock-in, and NL-G-F/MAPT double knock-in are used to understand pathophysiology of AD. All these mice vary in pathogenesis with different Aβ aggregate levels, NFT toxicity, disease progression, neuronal cell death, and cognitive impairment with aggressive amyloid deposition are also used to understand pathophysiological mechanisms leading to AD pathology<sup>10,12,13</sup>. However, these mice models with aggressive pathologies fail to include the effects of aging in neurodegeneration. Among the several AD mice models, APP<sup>SWE</sup>/PSEN1dE9 Tg (APP<sup>SWE</sup>/PS1 Tg) mice demonstrate comparatively mild phenotype with slow amyloid deposition, making these models more relevant to study the effects of aging in the AD disease progression<sup>10,12,13</sup>.

APP<sup>SWE</sup>/PS1 Tg mice have been extensively used to characterize and understand the neuronal changes in AD pathology. Several studies in APP<sup>SWE</sup>/PS1 Tg mice indicated the development of Aβ pathology as early as 6 months, neuronal loss at 8 months, and a decline in cognitive function at 12 months³. APP<sup>SWE</sup>/PS1 Tg mice demonstrate the development of fibrillar and neuritic plaques with increased neuroinflammation and irregulated adrenergic system<sup>12,14</sup>. APP<sup>SWE</sup>/PS1 Tg mice also demonstrated altered dendritic structure with decreased dendritic diameter without neuronal loss in the lateral nucleus of the amygdala<sup>15</sup>. In addition, APP<sup>SWE</sup>/PS1 Tg mice showed decreased neurogenesis with the development of pathology and synaptic dysfunction<sup>16</sup>. Studies also indicated disturbed vessel homeostasis in APP<sup>SWE</sup>/PS1 Tg mice, leading to cerebrovascular dysfunction contributing to cognitive impairment<sup>17</sup>. Aβ aggregates are also reported to localize in the mitochondria of APP<sup>SWE</sup>/PS1 Tg mice, causing increased oxidative stress and cholesterol accumulation in mitochondria<sup>18</sup>. Additionally, multiple studies documented that APP<sup>SWE</sup>/PS1 Tg mice develop age-related mitochondrial dysfunction with increased vulnerability to oxidative stress, altered energy metabolism with increased insulin resistance, impaired proteostasis, altered mitochondrial morphology with increased mitochondrial fission, and increased apoptosis<sup>19–23</sup>. All these pathologies, as mentioned above in APP<sup>SWE</sup>/PS1 Tg mice, are associated with the development of cognitive impairment and AD pathology<sup>9</sup>.

An ample number of existing literature demonstrates mice models of vascular dementia, aging, and senescence are associated with diastolic dysfunction with increased myocardial fibrosis  $^{24-26}$ . Additionally, protein aggregation in the myocardium is related to cardiac dysfunction. Existing studies demonstrate cardiac dysfunction in experimental models of cardiac amyloidosis due to the deposition of pre-amyloid oligomers (caused by ATTR or desmin mutation) $^{27-30}$ . Recently, we also reported cardiac dysfunction with increased cardiac fibrosis in  $\alpha$ B-Crystallin and Desmin-dependent models of cardiac proteotoxicity $^{30,31}$ . Besides these, some studies reported the development of diastolic dysfunction in AD patients. Initial studies demonstrated autonomic cardiac dysfunction in the electrocardiogram of AD patients, which was attributed to cholinergic deficits $^{32}$ . Subsequent investigations revealed diastolic dysfunction with altered transmitral blood flow and increased relaxation time (suggesting relaxation defects) $^{33-35}$  along with aortic stiffness measured by a higher stiffness index and lower stretchability $^{34}$  and an increase in intraventricular septum thickness in AD patients $^{36}$ . This cardiac dysfunction in AD patients was attributed mainly to the presence of intramyocardial  $\beta$ -amyloid aggregates $^{35}$ . In addition to A $\beta$  aggregates, the clumping of neurofibrillary tangles formed by accumulating hyperphosphorylated tau proteins also exhibits similar phenotypes with diastolic dysfunction  $^{37}$ .

Extensive studies on AD suggest APP localization and processing in neuronal cells, where it functions in helping neuronal development and providing protection against injury and aging, while knocking out APP increases the mortality after ischemia in mice<sup>38,39</sup>. Several groups have also shown APP expression in non-neuronal tissues, including blood vessels, skin, intestine, adipocytes, subcutaneous tissue, and muscle, which are responsible for different functions including but not limited to promoting cell adhesion with various extracellular matrix components, aiding in muscle development and synapse formation in the motor neurons, and many more<sup>40,41</sup>. Although a few studies demonstrated myocardial deposits of A $\beta$  aggregates the existence of cardiac anomalies in AD patients, none of the studies focused on the characterization of the experimental AD models for cardiac pathology and exploring the molecular mechanism responsible for cardiac dysfunction in AD mice (if any). Therefore, in this study, we first found A $\beta$  aggregate deposition in the hearts of aged APP<sup>SWE</sup>/PS1 Tg mice and explored the possible molecular and biochemical events associated with the cardiac dysfunction in these AD mice models. Here, we reported that APP<sup>SWE</sup>/PS1 Tg mice developed diastolic dysfunction with pathological remodeling and mitochondrial dysfunction with decreased mitochondrial complex activity, altered OXPHOS complex expression, altered mitochondrial antioxidant system, altered mitochondrial dynamics and proteostasis.

### Results

### Diastolic dysfunction in APPSWE/PS1 Tq hearts

Alzheimer's disease (AD) patients are diagnosed with the prevalence of cardiac dysfunction, especially with abnormal transmitral blood flow 33,35. Therefore, using non-invasive echocardiography, we used the aged APPSWE/PS1 Tg mice (24 months of age) and littermate control Wt mice to monitor cardiac function. M-mode echocardiographic measurement showed no significant changes in systolic cardiac function parameters including diastolic and systolic volumes (Fig. 1A–B), percent ejection fraction (%EF; Fig. 1C), left ventricular internal diameter (LVID) at both diastole and systole (Fig. 1D–E), percent fractional shortening (%FS; Fig. 1F), intraventricular septum (IVS) thickness at diastole (Fig. 1G), and left ventricular posterior wall (LVPW) thickness at diastole (Fig. 1H). Heart rate (Fig. 1I) measurement showed no significant difference in beats per minute across the groups.

We also assessed the LV diastolic function parameters using tissue and pulse wave Doppler measurements (Fig. 2). Mitral inflow velocity measurements showed a significant increase during early diastolic filling (E wave; MV E) in APPSWE/PS1 Tg mice compared to Wt controls (Fig. 2A) with no significant change during atrial contraction (A wave; MV A) (Fig. 2B), leading to an overall increases MV E/A ratio in APPSWE/PS1 Tg mice (Fig. 2C). Further analysis of the relative contribution of atrial contraction to diastolic filling displayed a significant decrease, suggesting restrictive filling in APPSWE/PS1 Tg mice (Fig. 2D). Further measurements for early diastolic mitral valve septal annulus velocity (MV IVS E') demonstrated no significant change across the groups (Fig. 2E), resulting in an increased relationship between early diastolic inflow and septal annulus velocity (E/E') (Fig. 2F). The changes in all these parameters indicated unusual diastolic filling, further suggesting diastolic dysfunction in aged APPSWE/PS1 Tg mice compared to age-matched littermate Wt mice. Additionally, we also evaluated the LV dyssynchrony using speckle tracking based strain measurements from B-mode echocardiography (Supplement Figure S1)<sup>26</sup>. Measurements for reverse longitudinal global strain showed a significant decrease (Supplement Figure S1A) and reverse radial global strain demonstrated significant increase (Supplement Figure S1B) during diastolic filling in APPSWE/PS1 Tg mice compared to Wt. Assessment of maximum time-to-peak (T2P) delay values for longitudinal strain (Supplement Figure S1C) and radial strain (Supplement Figure S1D) displayed no change across the groups. However, the standard deviation of T2P was significantly increased for longitudinal strain (Supplement Figure S1E) but remained unchanged for radial strain (Supplement Figure S1F). Furthermore, measurements for the standard deviation of the T2P/RR ratio showed a significant increase for longitudinal strain in APPSWE/PS1 Tg mice compared to Wt mice (Supplement Figure S1G) but remained unchanged for radial strain across the groups (Supplement Figure S1H). All these changes indicated LV dyssynchrony with LV deformation in APP<sup>SWE</sup>/PS1 Tg mice compared to age-matched littermate Wt controls.

## APP<sup>SWE</sup>/PS1 Tg mice exhibit skeletal muscle dysfunction with exercise intolerance and decreased muscle endurance

Skeletal muscle dysfunction with exercise intolerance is one of the primary symptoms of diastolic dysfunction. Additionally, cognitive decline is associated with decreased hand grip strength. Therefore, to corroborate the events in diastolic dysfunction and cognitive decline, we performed grip strength measurements (Fig. 3A–B) to assess muscle endurance and graded maximal exercise (Fig. 3C–F) to measure exercise tolerance. Grip strength measurements demonstrated significantly lower values for both absolute (Fig. 3A) and normalized (Fig. 3B) grip strength in APP<sup>SWE</sup>/PS1 Tg mice, suggesting decreased muscle endurance in APP<sup>SWE</sup>/PS1 Tg mice. Similarly, when subjected to forced treadmill exercise, APP<sup>SWE</sup>/PS1 Tg mice exhibited a significant decrease in time to exhaustion (Fig. 3C) and maximum distance covered (Fig. 3D) during the experiment, suggesting lower exercise tolerance in APP<sup>SWE</sup>/PS1 Tg mice. However, no significant difference was observed in the maximal (Fig. 3E) and average (Fig. 3F) speeds attained. The results indicated skeletal muscle dysfunction with reduced muscle endurance and exercise tolerance in aged APP<sup>SWE</sup>/PS1 Tg mice compared to age-matched littermate Wt mice.

### Aß-amyloid protein accumulates and forms aggregates in the heart

Existing studies demonstrated cardiac dysfunction in Alzheimer's Disease patients with intramyocardial deposition of amyloid aggregates in the heart<sup>35</sup>. Therefore, we assessed the expression of A $\beta$ -amyloid in the left ventricular myocardium in whole cell lysates and the tissue sections from APPSWE/PS1 Tg and found that A $\beta$ -amyloid protein is expressed in the cardiac tissue (Fig. 4). Western blot analysis showed the presence of full-length APP and APP-breakdown products in the APPSWE/PS1 Tg hearts (Fig. 4A). A $\beta$ -amyloid expression in the LV myocardium was further confirmed using immunohistochemistry as indicated by the patchy brown stain in the APPSWE/PS1 Tg myocardial sections (Fig. 4B). Immunostaining of the LV myocardial sections from APPSWE/PS1 Tg mice hearts for A $\beta$ -amyloid displayed amyloid aggregate formation in the cardiomyocytes (Fig. 4C). We also confirmed the presence of amyloid oligomers in the APPSWE/PS1 Tg hearts using an oligomer-specific A11 antibody<sup>42</sup> (Fig. 4D). Overall, the APPSWE/PS1 Tg hearts showed the presence of full-length APP and APP-breakdown products, amyloid deposition, and toxic amyloid oligomers.

# APP<sup>SWE</sup>/PS1 Tg hearts developed histopathological remodeling with increased fibrosis and cardiac hypertrophy

As the APP<sup>SWE</sup>/PS1 Tg mice developed cardiac diastolic dysfunction and the presence of toxic amyloid oligomers, we evaluated the hearts for histopathological remodeling. Picro-Sirius Red staining of the LV myocardial sections demonstrated increased collagen content in APP<sup>SWE</sup>/PS1 Tg mice (Fig. 5A). Additionally, cross-sectional area (CSA) measurements of the cardiomyocytes analyzed from WGA-stained tissue sections showed significantly higher CSA in aged APP<sup>SWE</sup>/PS1 Tg mice compared to age-matched littermate Wt mice (Fig. 5B). We also assessed the hearts for changes in inflammation and ECM degradation markers. We found no significant changes

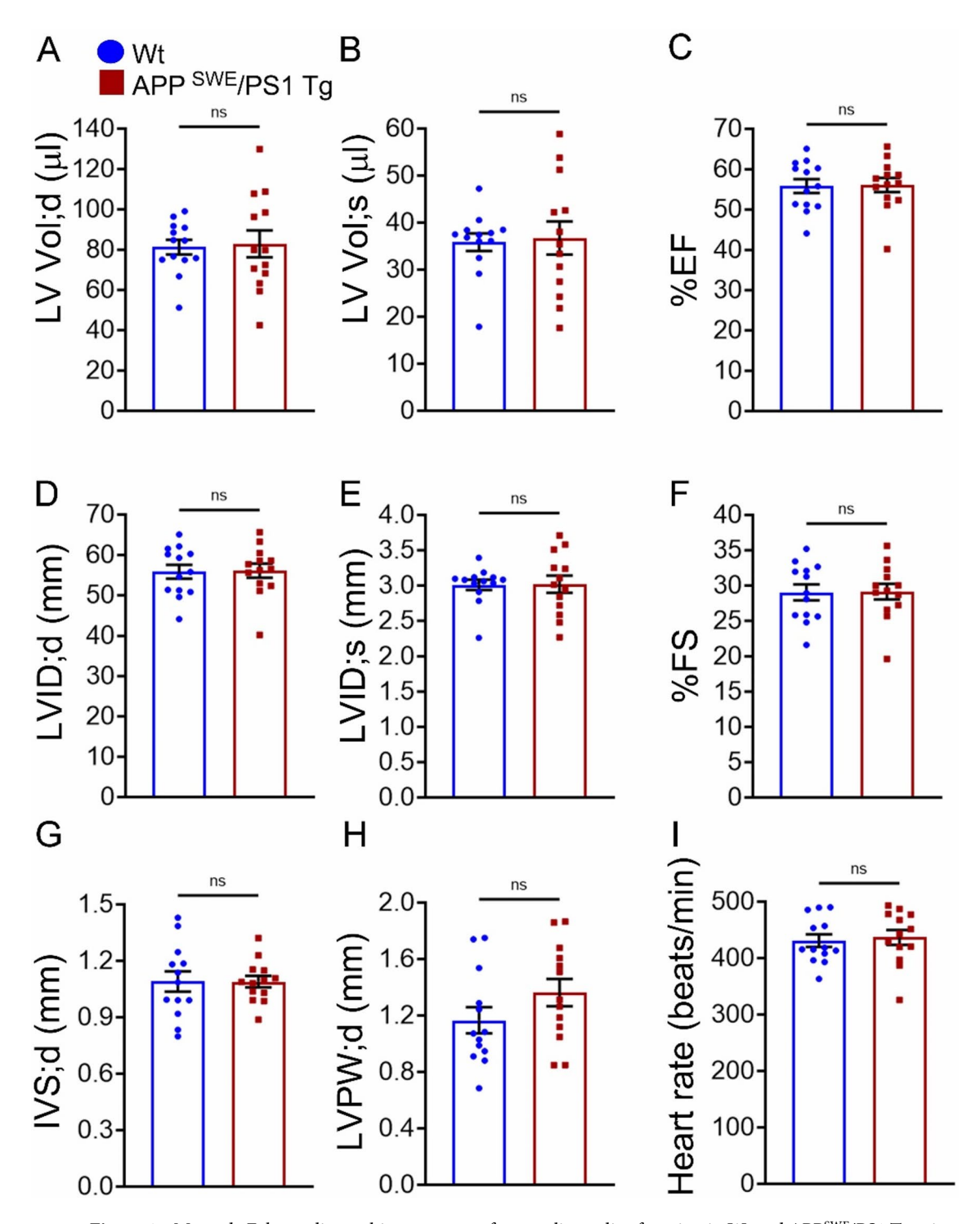


**Figure 1.** M-mode Echocardiographic parameters for systolic cardiac function in Wt and APP<sup>SWE</sup>/PS1 Tg mice. (**A**)–(**I**) M-mode echocardiographic indices for cardiac function indicate a similar systolic function in APP<sup>SWE</sup>/PS1 Tg compared to age-matched littermate Wt controls. (**A**) Diastolic Left Ventricular (LV) Volume (LV Vol; d). (**B**) Systolic Left Ventricular Volume (LV Vol; s). (**C**) Percent Ejection Fraction (%EF). (**D**) Left Ventricular Internal Diameter at diastole (LVID; d). (**E**) Left Ventricular Internal Diameter at systole (LVID; s). (**F**) Percent Fractional Shortening (%FS). (**G**) LV Intraventricular septum thickness at diastole (IVS; d). (**H**) Diastolic LV posterior wall thickness (LVPW; d). (**I**) Heart rate (beats/min) (n = 13 mice per group). Bar graphs represent mean ± SEM. Each dot in the graph corresponds to individual data points from each mouse. An unpaired Student *t*-test was used to determine the *p* values. *ns*, Not significant; Wt, Wildtype.

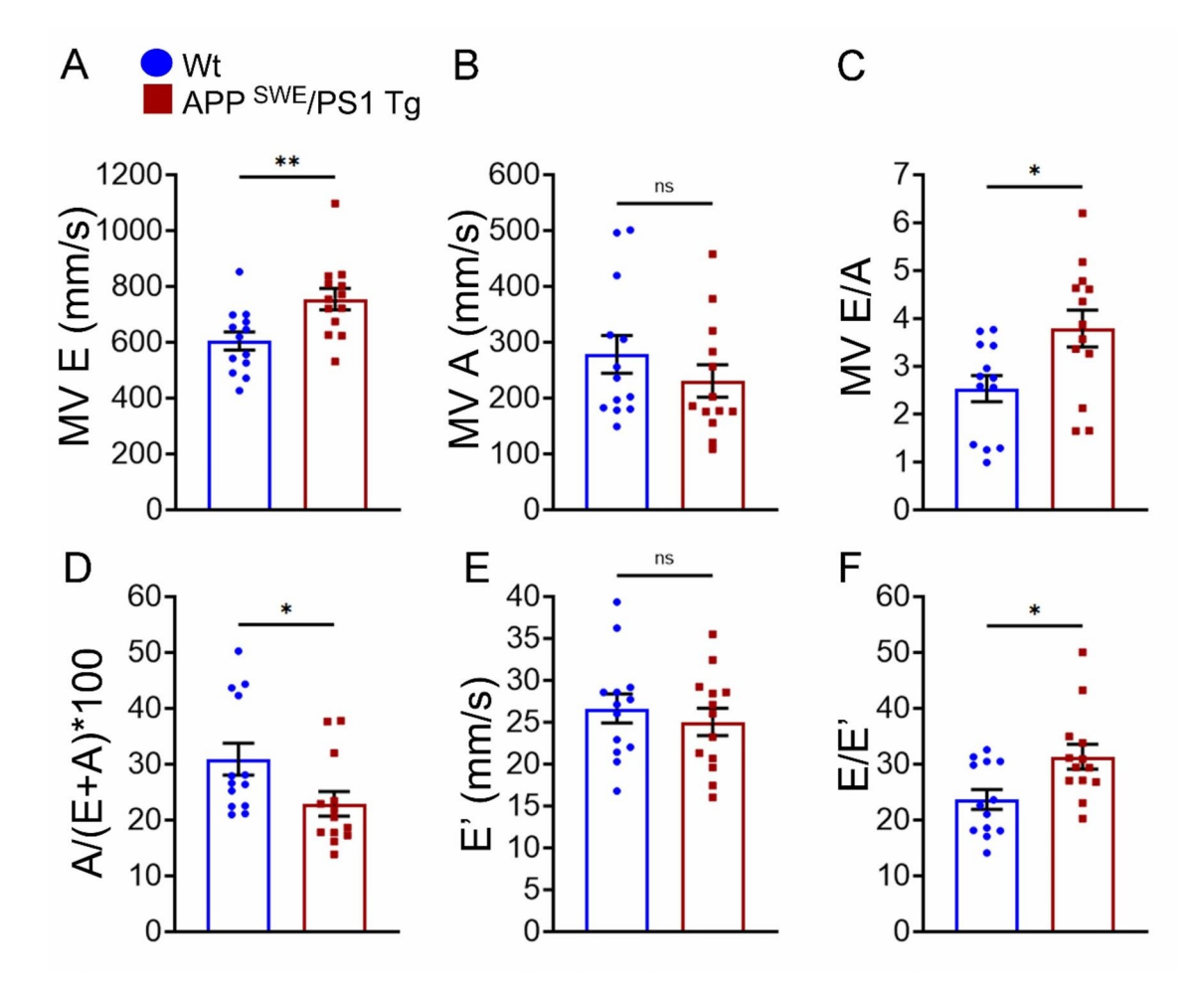


**Figure 2.** Tissue and Pulse wave Doppler parameters for diastolic cardiac function in Wt and APP<sup>SWE</sup>/PS1 Tg mice. (**A**)–(**F**) Tissue Doppler and Pulse wave Doppler parameters for cardiac function suggest diastolic dysfunction in APP<sup>SWE</sup>/PS1 Tg compared to age-matched littermate Wt controls. (**A**) Mitral inflow velocity during early diastolic filling (E-wave; MV E). (**B**) Mitral inflow velocity during atrial contraction (A-wave; MV A). (**C**) The ratio for absolute values of early-to-late diastolic flow velocity (MV E/A). (**D**) Percent contribution of atrial contraction to diastolic filling. (**E**) Early diastolic mitral annular velocity at septal (IVS) wall (E'). (**F**) Relationship between early diastolic mitral inflow velocity and diastolic mitral annular velocity at septal (IVS) wall (E/E') (n = 13 mice per group). Bar graphs represent mean  $\pm$  SEM. Each dot in the graph corresponds to individual data points from each mouse. An unpaired Student *t*-test was used to determine the *p* values. \*p < 0.05; \*p < 0.01; ns, Not significant; Wt, Wildtype.

in the protein levels for phosphorylated NF $\kappa$ B and MMP2 between genotypes (Supplement Figure S2A–C). Hematoxylin and eosin staining for the myocardial sections showed no notable changes between the APP<sup>SWE</sup>/PS1 Tg and Wt hearts (Supplement Figure S2D).

# Altered levels of cellular antioxidants, mitochondrial dynamics, and mitochondrial proteostasis regulatory proteins in APP<sup>SWE</sup>/PS1Tg hearts

Increased oxidative stress and altered mitochondrial dynamics were reported to be associated with the development of AD pathology<sup>43</sup>. Previous studies also indicated higher oxidative damage with altered antioxidant systems in the brains of human AD patients and mouse models of AD<sup>44,45</sup>. However, the antioxidant levels in the AD hearts remain unexplored. Therefore, we evaluated the changes in the antioxidant system in these mice and found a significant decrease in Catalase and SOD1 in aged APP<sup>SWE</sup>/PS1 Tg mice compared to age-matched littermate Wt mice (Fig. 6A,B). However, the protein levels of Glutathione peroxidase (Gpx1) and MnSOD remained unchanged (Fig. 6A,B). Similarly, quantification of the protein levels of DNA damage markers (e.g. 8-OHdG) and DNA damage sensing markers (e.g. ATM and ATR) in whole cell lysate of Ntg and APP<sup>SWE</sup>/PS1Tg mice did not show any significant change across the groups (Supplement Figure S3).

Previous studies demonstrated altered mitochondrial dynamics in neuronal samples from both in vitro and in vivo models of AD<sup>46-48</sup>, and showed that altered oxidative stress facilitates changes in mitochondrial dynamics<sup>4</sup>. Therefore, we evaluated changes in mitochondrial dynamics regulatory proteins and found a significant decrease in mitochondrial fission regulators (Drp1 and Fis1) in aged APP<sup>SWE</sup>/PS1 Tg hearts (Fig. 6A,C). Similarly, mitochondrial fission activating phosphorylation of Drp1 (pDrp1Ser616) was also significantly reduced in APP<sup>SWE</sup>/PS1 Tg hearts (Fig. 6A,C).

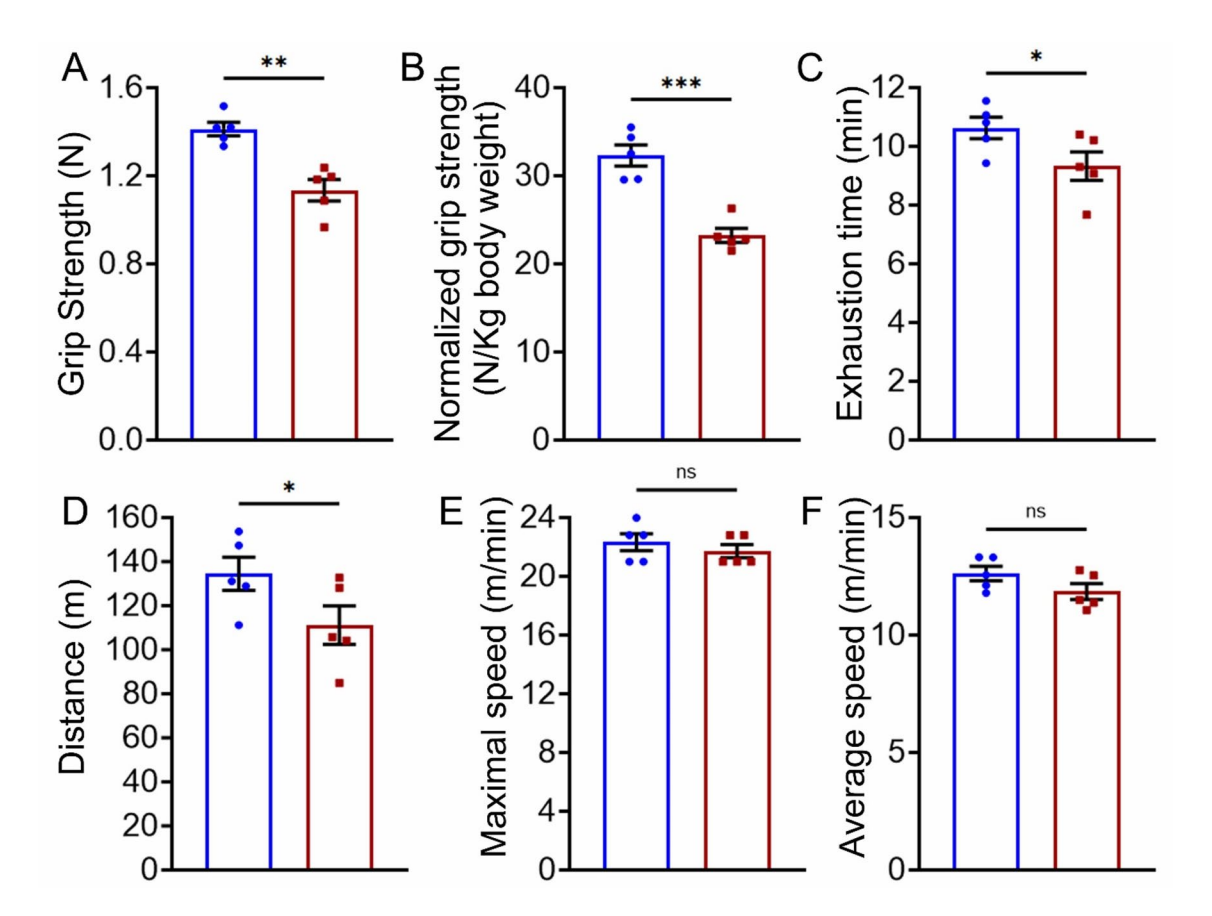


**Figure 3.** Reduced skeletal muscle endurance and exercise tolerance in APP<sup>SWE</sup>/PS1 Tg mice. (**A**)–(**B**) Grip strength measurements show decreased endurance in the skeletal muscles of APP<sup>SWE</sup>/PS1 Tg mice compared to age-matched littermate Wt controls. (**A**) Absolute Grip strength (N). (**B**) Grip strength normalized to body weight (N/Kg body weight). (**C**)–(**F**) Forced exercise measurements suggest decreased exercise tolerance in APP<sup>SWE</sup>/PS1 Tg mice compared to age-matched littermate Wt controls. (**C**) Exhaustion time (min). (**D**) Maximum distance covered (m). (**E**) Maximum speed attained (m/min). (**F**) Average speed (m/min) (n = 5 mice per group). Bar graphs represent mean  $\pm$  SEM. Each dot in the graph corresponds to individual data points from each mouse. An unpaired Student *t*-test was used to determine the *p* values. \* p < 0.05; \*\* p < 0.01; \*\*\* p < 0.001; NS, Not significant; Wt, Wildtype.

PS1 Tg hearts, while mitochondrial fission inhibiting phosphorylation of Drp1 (pDrp1Ser637) was dramatically increased in APP<sup>SWE</sup>/PS1 Tg hearts (Fig. 6A,C). Interestingly, we also found a significant decrease in inner mitochondrial membrane fusion regulatory protein OPA1 while Mfn2 (outer mitochondrial membrane fusion regulatory protein) remain unchanged (Fig. 6A,C).

Mitochondrial proteostasis plays an important role in the clearance of protein aggregates and dysfunctional mitochondria. Loss of mitochondrial proteostasis is widely associated with several neurodegenerative diseases including AD<sup>49–51</sup>. Therefore, we evaluated the changes in levels of different proteases and found a significant decrease in serine proteases located in mitochondrial intermembrane space (HtrA2), matrix (LonP1 and ClpP), and Hsp60 (Fig. 6A,D). The expression levels of other proteases, including Sam50, Hsc70, paraplegin, and Oma1 (inner membrane serine protease) remained unchanged (Fig. 6A,D).

# Mitochondrial dysfunction with altered $\it electron$ transport chain and decreased mitochondrial bioenergetics in APP Hearts

Mitochondrial dysfunction with respiratory defects and oxidative damage in AD brains is well evident in the literature. However, none of the studies explored the changes in the cardiac mitochondria of AD incidences. Moreover, previous studies from our lab have shown mitochondrial dysfunction with altered mitochondrial dynamics, hyperactive mitochondrial fission, and decreased mitochondrial fusion in mice models of cardiac proteotoxicity<sup>30,31</sup>. Therefore, we assessed mitochondrial oxidative phosphorylation capacity at protein levels by evaluating the complex activities and mitochondrial bioenergetics. Evaluation of OXPHOS and PDH protein levels in the whole cell fraction exhibited a significant decrease in protein expression of Complexes I, II, and III subunits (Fig. 7A,B) and E2 subunit (Fig. 7A,C), respectively. However, protein expression of Complex V of OXPHOS protein complex (Fig. 7A,B), and E3bp and E1 $\alpha$ / $\beta$  subunit of PDH protein complex (Fig. 7A,C) remained unchanged across the groups. The function of the mitochondrial electron transport system largely depends on the assembly and dynamics of the five complexes involved, forming different supercomplexes (SCs) together. Therefore, we evaluated the changes in mitochondrial supercomplexes and the subunits in their native

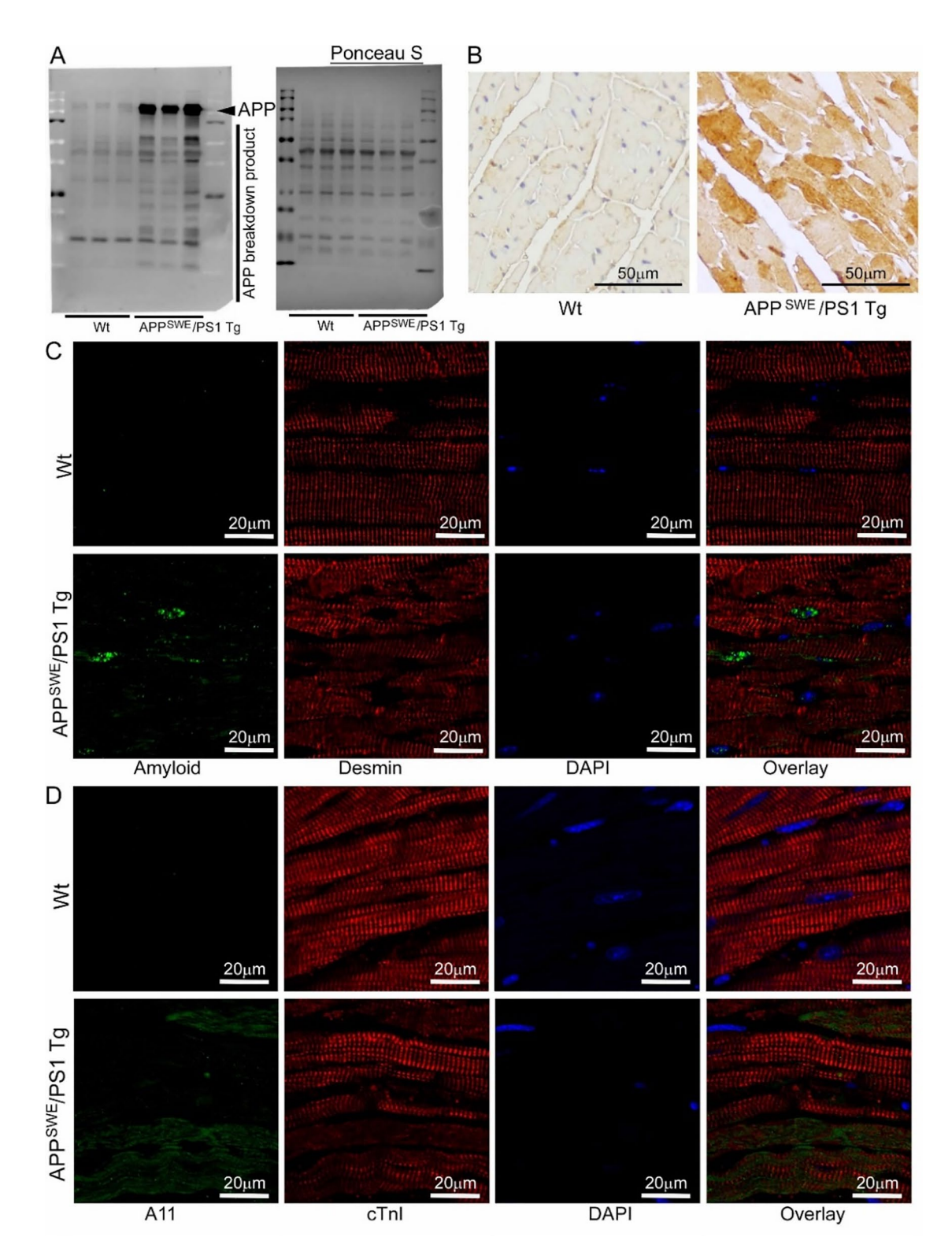


**Figure 4.** Accumulation of Aβ-amyloid protein aggregates in the heart. (**A**) Representative Western Blot for Aβ-amyloid protein in the whole cell lysate from the hearts of Wt and APP<sup>SWE</sup>/PS1 Tg mice. Ponceau S staining of the membrane after transfer was used to confirm equal loading of the samples across the wells (n = 3 mice per group). (**B**) Representative brightfield images for IHC-staining for Aβ-amyloid in the paraffin-fixed heart tissue sections from Wt and APP<sup>SWE</sup>/PS1 Tg mice. Hematoxylin (blue) was used to counterstain the nuclei (n = 4 mice per group). Scale bars: 50 μm. Representative immunofluorescence image showing the presence of (**C**) Aβ-amyloid (green) and (**D**) amyloid oligomers by staining with an oligomer-specific A11 antibody (green) observed in paraffin-fixed APP<sup>SWE</sup>/PS1 Tg heart sections. Desmin (red) and cardiac Troponin I (red) were used as a counterstain for cardiomyocytes, and DAPI (blue) was used to counterstain nuclei (n = 4 mice per group). Scale bars: 20 μm. Wt, Wildtype.

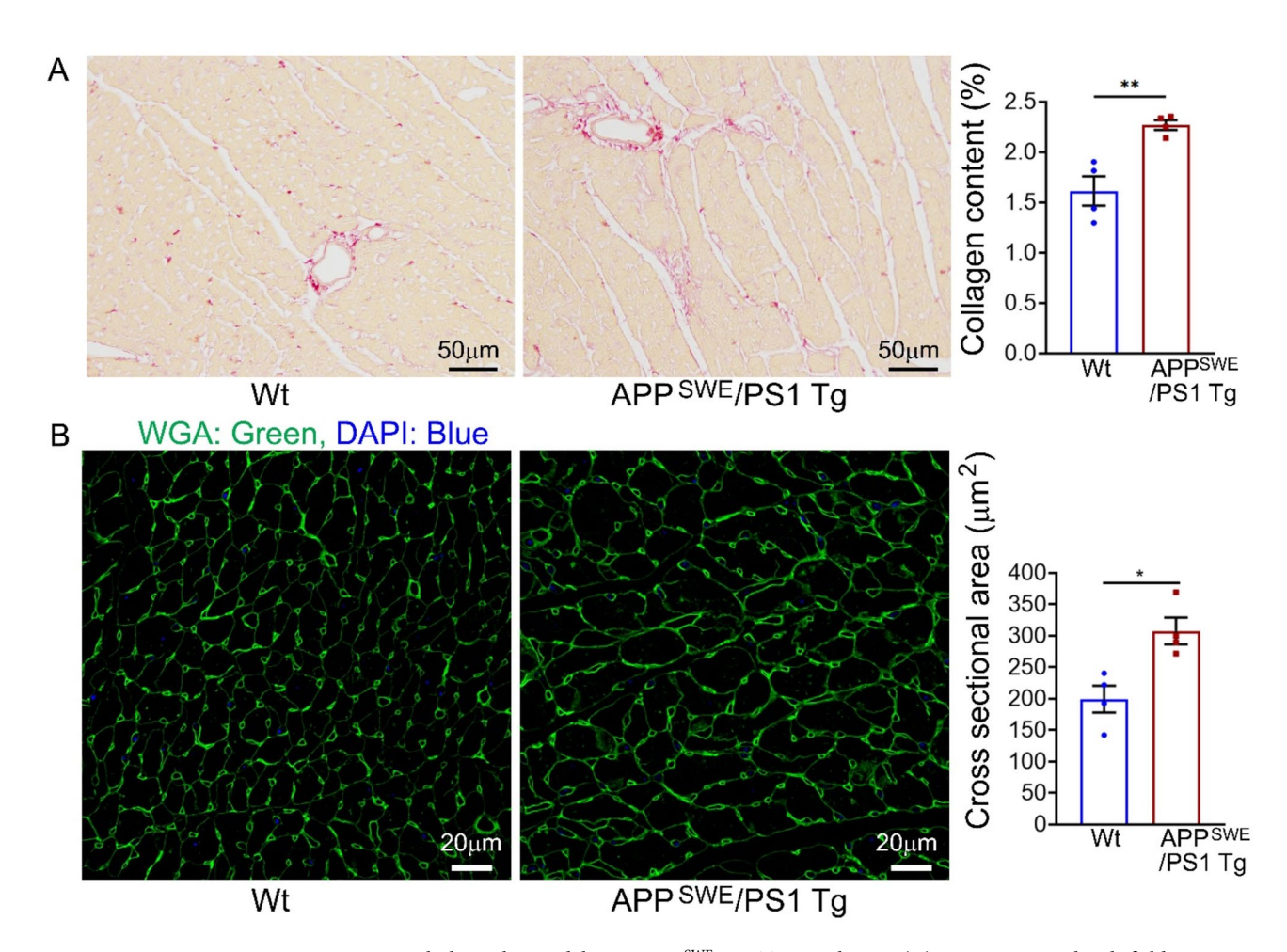


**Figure 5.** Histopathological remodeling in APP<sup>SWE</sup>/PS1 Tg mice hearts. (**A**) Representative brightfield micrographs of Picro-Sirius red-stained LV myocardial cross-sections for collagen deposition (red stain) (left panel) in Wt and APP<sup>SWE</sup>/PS1 Tg mice and its respective quantification for percent collagen deposition (right panel) showing increased collagen deposition in APP<sup>SWE</sup>/PS1 Tg heart sections (>17 images quantified per mice per group; n=4 mice per group). Scale bars: 50  $\mu$ m. (**B**) Representative immunofluorescence images of wheat germ agglutinin (WGA)-stained (green) paraffin-fixed LV myocardial sections from Wt and APP<sup>SWE</sup>/PS1 Tg mice (left panel) and the respective quantification for cardiomyocyte cross-sectional area (CSA) (right panel) showing increased CSA in APP<sup>SWE</sup>/PS1 Tg hearts. (>10 images quantified per mice per group; n=4 mice per group). Scale bars: 20  $\mu$ m. Bar graphs represent mean ± SEM. Each dot in the graph corresponds to individual data points from each mouse. An unpaired Student t-test was used to determine the p values. \*p < 0.05; and \*\*p < 0.01; Wt, Wildtype.

form and found significant changes in supercomplex dynamics with increased disintegration of complex I and V. In contrast, complex IV and II were significantly lower in APPSWE/PS1 Tg hearts mitochondria (Fig. 7D,E). We assessed the complex I, II, and III activities to ascertain if the changes in complex I, II and III expression and supercomplexes dynamics affected the individual activities of mitochondrial complexes (Fig. 7F-H). We found a significant decrease in complex I and III activities in APPSWE/PS1 Tg hearts (Fig. 7F,H). Despite a significant reduction in protein expression in the whole cell fraction of APPSWE/PS1 Tg hearts (Fig. 7A,B), the complex II activity remained unchanged across the groups (Fig. 7G).

We also evaluated the changes in mitochondrial bioenergetics in APP<sup>SWE</sup>/PS1 Tg and control hearts (Fig. 8). We found a significantly lower oxygen consumption rate (OCR) profile in mitochondrial fraction from APP<sup>SWE</sup>/PS1 Tg hearts (Fig. 8A). The quantification for OCR at baseline, which includes the sum of all the physiological oxygen consumption by mitochondria, revealed significantly lower basal respiration in APP<sup>SWE</sup>/PS1 Tg hearts (Fig. 8A,B). Inhibition of ATP synthase (Complex V) using oligomycin shuts down mitochondrial ATP synthesis, causing a drop in OCR and allowing the calculation of ATP-linked OCR. Assessment of ATP-linked OCR demonstrated significantly lower values in APP<sup>SWE</sup>/PS1 Tg mitochondria compared to the control mitochondria (Fig. 8A,C). Following oligomycin, carbonyl cyanide-p-trifluoromethoxy-phenylhydrazone (FCCP) was injected to uncouple the mitochondrial proton gradient and allow for maximal oxygen consumption. Analysis for FCCP-coupled OCR demonstrated a similar significant decrease in respiration values in mitochondria from APP<sup>SWE</sup>/PS1 Tg heart (Fig. 8A,D). Injection of rotenone and antimycin A (Complexes I and III inhibitors, respectively) completely shut down mitochondrial respiration, and the remaining OCR values correlate to non-mitochondrial respiration. Quantification for non-mitochondrial respiration in APP<sup>SWE</sup>/PS1 Tg and control mitochondria

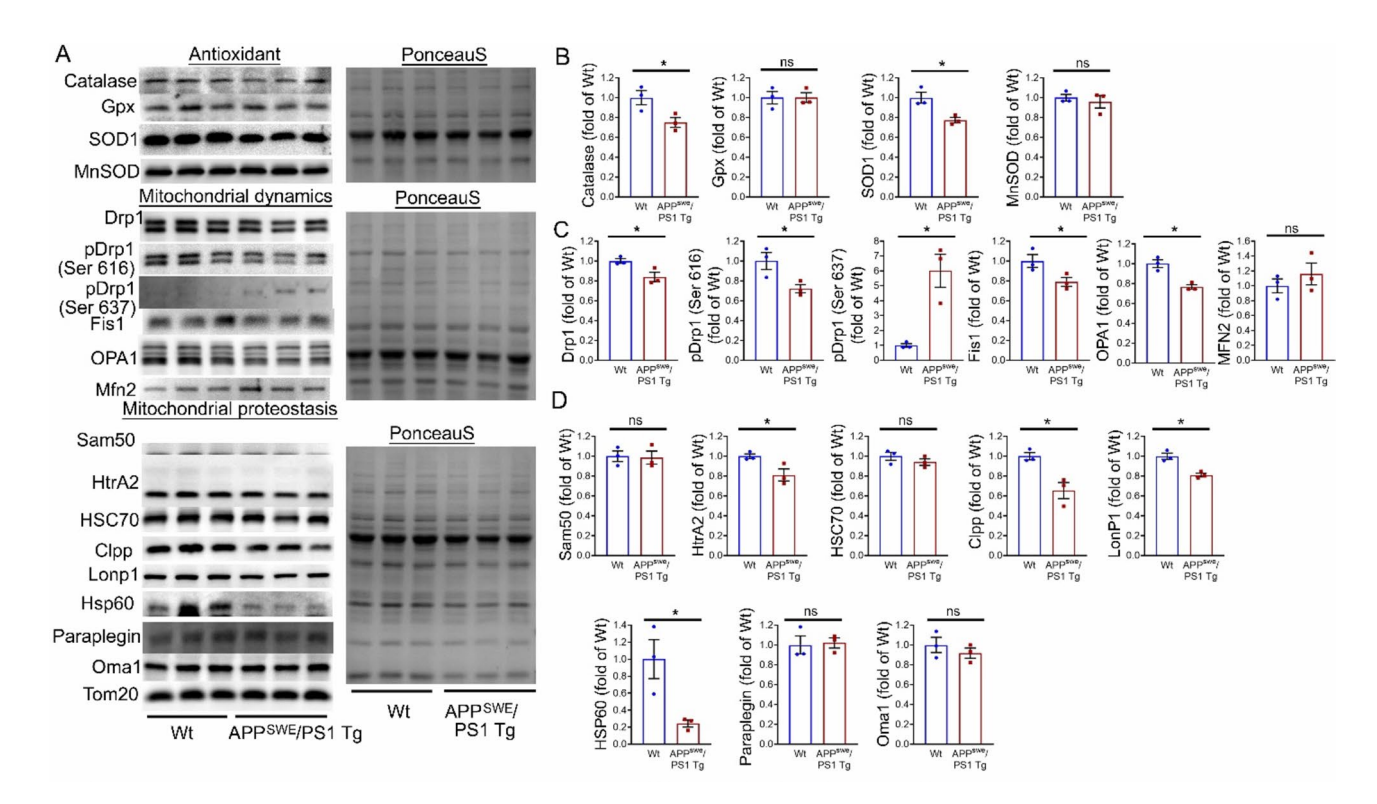
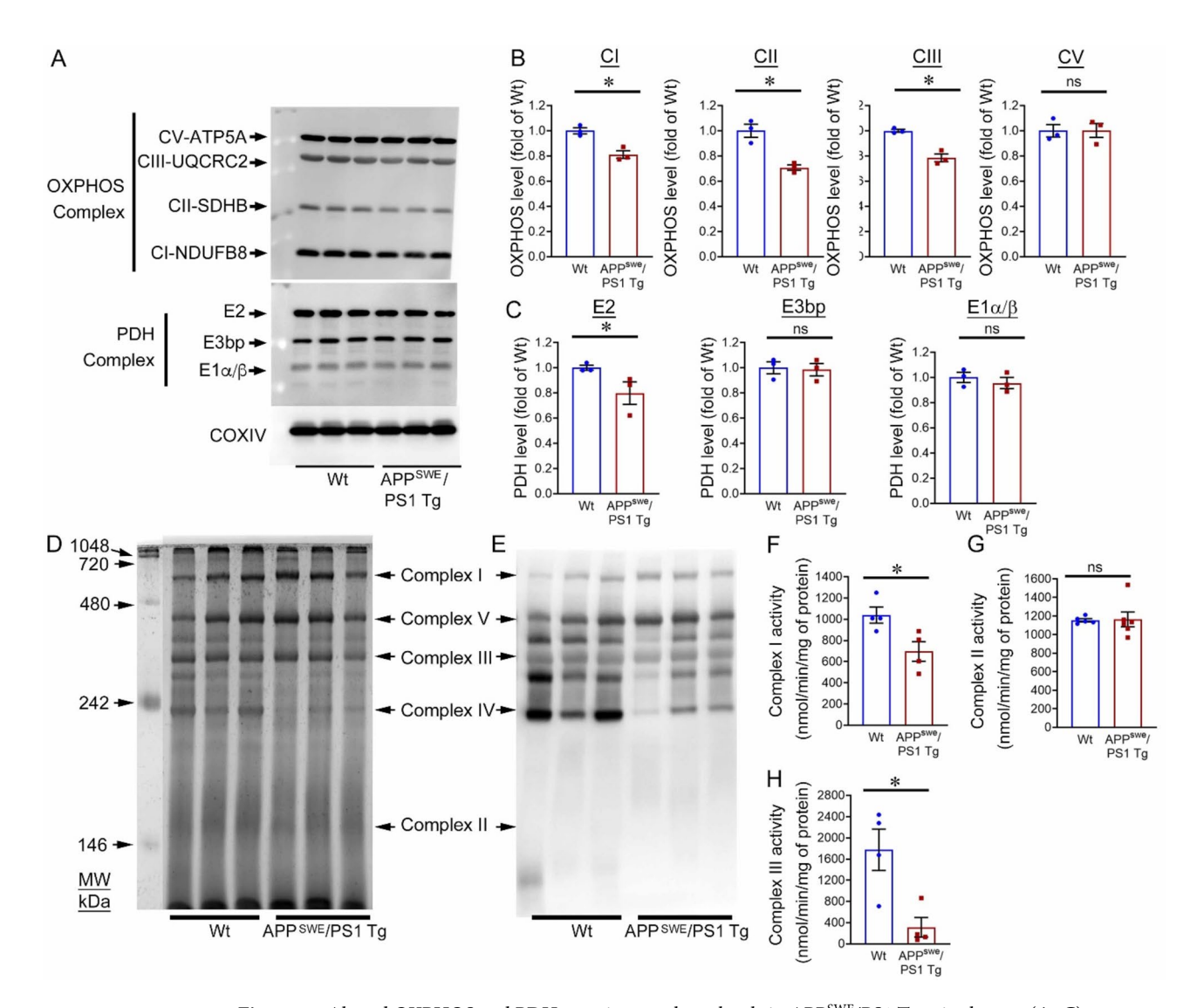


Figure 6. Altered antioxidant, mitochondrial dynamics, and proteostasis regulatory protein levels in APPSWE/ PS1 Tg mice hearts. (A, B) Representative Western Blot images and their respective densitometric quantification for the expression of cellular and mitochondrial antioxidant proteins including Catalase, Glutathione Peroxidase1 (Gpx1), Superoxide Dismutase 1 (SOD1), and Manganese Superoxide Dismutase (MnSOD, also known as SOD2) in the whole cell lysate from the hearts of Wt and APPSWE/PS1 Tg mice. PonceauS staining of the membranes after transfer was used to confirm the equal loading of the proteins (n = 3 mice per group) (A, C) Representative Western Blot images and their respective densitometric quantification for the expression of proteins involved in regulating mitochondrial dynamics (mitochondria fission (Drp1, pDrp1 Ser616, pDrp1 Ser637, and Fis1), and mitochondrial fusion (OPA1, and Mfn2) in the whole cell lysate from the hearts of Wt and APP $^{\text{SWE}}$ /PS1 Tg mice. PonceauS staining was used to confirm the equal loading of the proteins (n = 3 mice per group). (A, D) Representative Western Blot images and their respective densitometric quantification for the expression of proteins involved in mitochondrial proteostasis in the whole cell lysate from the hearts of Wt and APPSWE/PS1 Tg mice. PonceauS staining was used to confirm the equal loading of the proteins (n = 3 mice per group). Bar graphs represent mean ± SEM. Each dot in the graph corresponds to individual data points from each mouse. The non-parametric Kruskal-Wallis test was used to determine p values. \*p < 0.05; NS, Not significant; Wt, Wildtype.

exhibited similar values across the groups (Fig. 8A,E). Next, the reserve capacity, i.e. the extra amount of energy produced in time of need, was calculated as a difference between FCCP-linked OCR and basal respiration. Upon calculation, we found a significantly reduced reserve capacity in APPSWE/PS1 Tg mitochondria (Fig. 8F). Similarly, when calculated for ATP turnover as the difference between basal OCR and ATP-linked OCR, APPSWE/PS1 Tg mitochondrial fraction displayed lower values than the Wt mitochondria (Fig. 8G). Lastly, maximal respiration, calculated by deducting non-mitochondrial respiration from FCCP-linked respiration, also demonstrated significantly lower values in APPSWE/PS1 Tg mitochondria compared to the control mitochondria (Fig. 8H). We found that APPSWE/PS1 Tg hearts exhibited mitochondrial dysfunction with decreased complexes I, II, and III protein expression, complexes I and III activities, and decreased mitochondrial respiration.

### Discussion

This study aimed to explore whether the commonly used mouse models of AD develop any pathological changes in heart function and assess the molecular alterations in the cardiac muscle. Existing studies demonstrated cardiac dysfunction with altered diastolic function owing to altered transmitral blood flow and aortic stiffness with intramyocardial deposition amyloid aggregates<sup>33–35</sup>. Several mice models exist to understand the pathophysiology of AD; however, these studies primarily focus on neuronal changes<sup>12</sup>. Despite the presence of diastolic dysfunction in AD, very few studies attempted to characterize cardiac dysfunction in AD mice models. Therefore, here we performed detailed histopathological characterization of AD hearts using APP<sup>SWE</sup>/PS1 Tg as the mice model and found several novel and intriguing results as follows: (i) APP<sup>SWE</sup>/PS1 Tg mice exhibited diastolic cardiac dysfunction with higher diastolic filling and significantly increased E/E' ratio and altered speckle-tracking-based strain parameters, (ii) APP<sup>SWE</sup>/PS1 Tg displayed reduced muscle endurance and exercise intolerance, (iii) myocardium showed the presence of ubiquitous and ununiform APP aggregates in the APP<sup>SWE</sup>/PS1 Tg hearts,



**Figure 7.** Altered OXPHOS and PDH protein complexes levels in APP<sup>SWE</sup>/PS1 Tg mice hearts. (**A–C**) Representative Western Blot images and the densitometric quantification for the expression of OXPHOS (**A,B**) and PDH (**A,C**) protein complexes in the whole cell lysate from the hearts of Wt and APP<sup>SWE</sup>/PS1 Tg mice. COXIV expression was used to confirm equal loading of the samples across the wells (n = 3 mice per group). (**D**) Representative image of Coomassie blue-stained non-gradient native polyacrylamide gel (6%) on freshly isolated mitochondrial fraction from Wt and APP<sup>SWE</sup>/PS1 Tg mice to observe changes in Electron Transport Chain (ETC) supercomplexes' assembly and abundance (n = 3 (1 male and 2 females) mice per group). (**E**) Representative Western Blot image for the expression of OXPHOS protein on the native gel subjected to BNPAGE followed by transfer to PVDF membrane (n = 3 mice per group). (**F,G**, and **H**) Activity assays mitochondrial complex I (**F**), II (**G**), and III (**H**) in the mitochondrial isolates from the hearts of Wt and APP<sup>SWE</sup>/PS1 Tg mice (n = 4 mice per group). Bar graphs represent mean ± SEM. Each dot in the graph corresponds to individual data points from each mouse. The non-parametric Kruskal–Wallis test was used to determine *p* values. \*p <0.05; NS, Not significant; Wt, Wildtype.

(iv) histopathological evaluation demonstrated increased collagen deposition (Picro-Sirius Red staining), and increased cross-sectional area (WGA staining) in APP<sup>SWE</sup>/PS1 Tg hearts, (v) Western blot analysis demonstrated altered antioxidants level, mitochondrial dynamics, and mitochondrial proteostasis in whole cell lysates from APP<sup>SWE</sup>/PS1 Tg hearts, (vi) mitochondrial dysfunction with altered OXPHOS and PDH protein levels, decreased Complex I and II activities, altered mitochondrial supercomplex dynamics, and reduced mitochondrial bioenergetics in APP<sup>SWE</sup>/PS1 Tg hearts.

Heart and brain form a functional continuum where neurodegenerative diseases affect the heart, and cardiovascular dysfunction can alter neuronal functions. Several studies have indicated increased cognitive decline and dementia in hypo-perfusion incidences, including myocardial ischemia<sup>52,53</sup>. Conversely, cardiovascular dysfunction is also evident in neurodegenerative diseases like Alzheimer's disease (AD) patients. Existing studies have primarily demonstrated diastolic dysfunction with altered transmitral blood flow, diastolic stiffness, and altered contraction. According to the A $\beta$  hypothesis, many of these changes are attributed to the intramyocardial

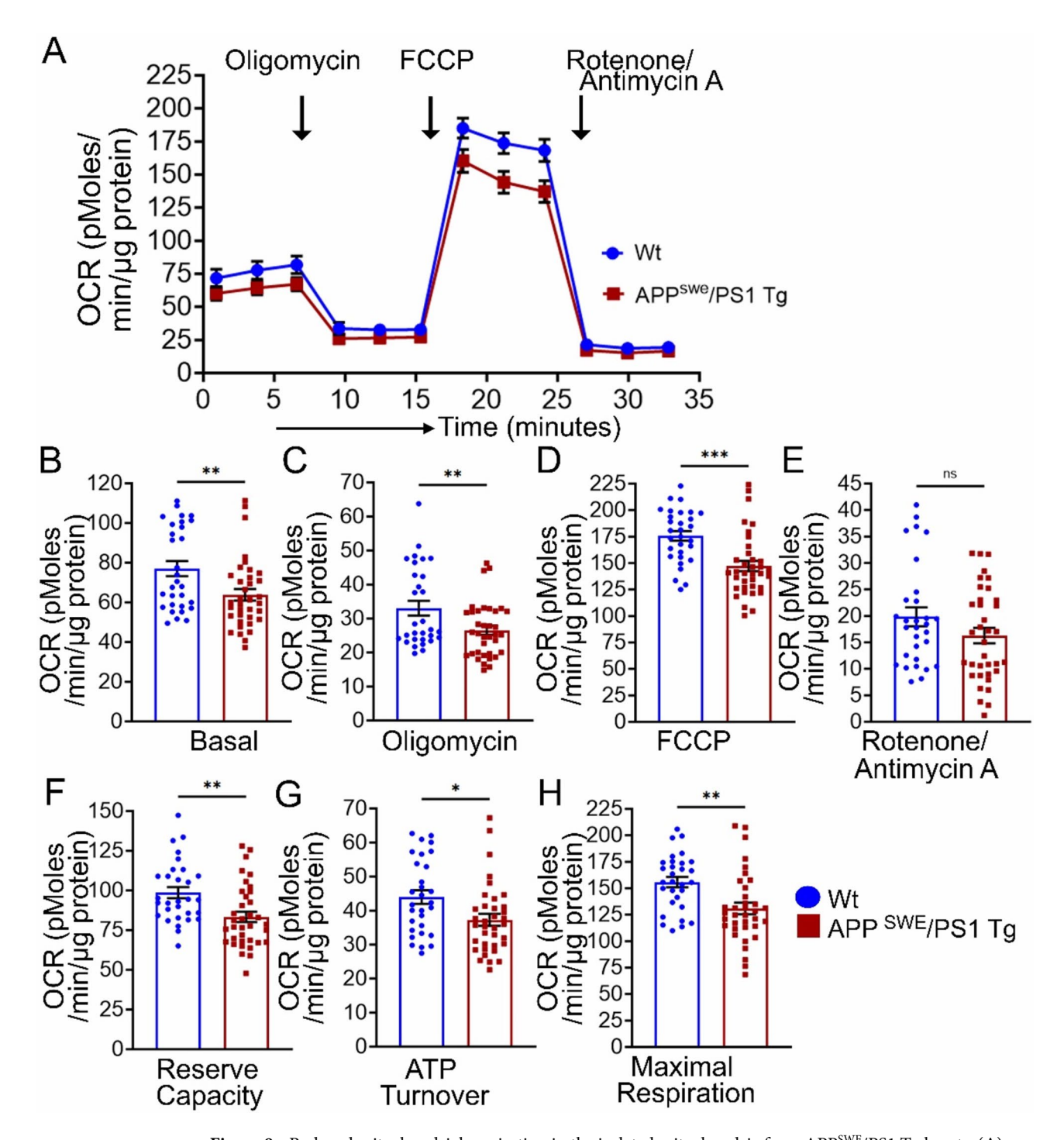


**Figure 8.** Reduced mitochondrial respiration in the isolated mitochondria from APP<sup>SWE</sup>/PS1 Tg hearts. (**A**) Oxygen consumption rate (OCR) curve for freshly isolated mitochondrial fraction from Wt and APP<sup>SWE</sup>/PS1 Tg hearts obtained by sequential addition of oligomycin (1 μmol/L), carbonyl cyanide-4-phenylhydrazone (FCCP) (2 μmol/L), and rotenone (0.5 μmol/L) plus antimycin A (0.5 μmol/L) (indicated by arrows). Each point on the curve represents the average of the OCR values from each mouse (n = 5 mice per group). OCR value is expressed as picomoles/min/μg protein. (**B-H**) Graphs for OCR values of respiratory parameters including (**B**) Basal respiration and after the addition of (**C**) Oligomycin, (**D**) FCCP, and (**E**) Rotenone and Antimycin A. Major respiratory parameters for mitochondrial function including (**F**) Reserve Capacity, (**G**) ATP Turnover, and (**H**) Maximal Respiration was calculated from the OCR values obtained in B to E in mitochondria isolated from Wt and APPSWE/PS1 Tg hearts (n = 5 mice per group). Bar graphs represent mean ± SEM. Each dot in the graph corresponds to the individual data point in the experiment. An unpaired Student *t* test was used to determine the *p* values. \*p < 0.05; \*\*p < 0.05; \*\*p < 0.01; and \*\*\*p < 0.001; ns, not significant; Wt, Wildtype.

deposition of amyloid aggregates<sup>35</sup>. However, few studies indicate that mutation in PSEN1 and 2<sup>54</sup>, and deposition of tau aggregates also cause idiopathic dilated cardiomyopathy with abnormal cardiac function 54,55. The presence of cardiac dysfunction in AD patients increases the risk of heart failure and other cardiac comorbidities, which makes it vital to understand the pathophysiology and the molecular mechanism behind the myocardial changes. Despite the existence of several mice models, most of the studies exploring cardiovascular dysfunction in AD patients are based on clinical data and samples, restricting the extensive evaluation of the mechanism. Very few studies have attempted to investigate the causative mechanism of cardiac dysfunction in AD extensively. Previous study also showed cardiac dysfunction with decreased contractile function with reduced %FS, increased fibrosis, and decreased mitochondrial respiration in 5XFAD mice<sup>56</sup>. The group suggested that all these changes were due to increased systemic levels of  $A\beta^{56}$ . Contrastingly, another study using the tau hyperphosphorylation model of AD recently reported no differences in systolic parameters (e.g., %FS) but comparatively higher diastolic parameters (e.g., E/A and E/E'). In line with the existing studies, our study demonstrated the development of cardiac diastolic dysfunction with altered mitral inflow velocity and restricted ventricular filling and no change in systolic function in APP<sup>SWE</sup>/PS1 Tg mice at 24 months of age, which correlates to the changes seen in human AD patients and tau model of proteotoxicity. Moreover, APP<sup>SWE</sup>/PS1 Tg hearts also demonstrated LV diastolic dysfunction, dyssynchrony, and deformity with decreased reverse longitudinal and increased radial strain, increased STD of T2P and T2P/RR ratio. Additionally, APPSWE/PS1 Tg hearts also displayed ubiquitous non-uniform deposition of Aβ aggregates in the myocardium, correlating with intramyocardial deposition of amyloid aggregates observed in AD hearts35,54.

Decreased skeletal muscle function and cardiac dysfunction in AD may be due to the accumulation of dysfunctional mitochondria and increased oxidative stress. Multiple studies have shown abnormal mitochondrial function as a leading cause of cardiac dysfunction. Several studies, including our previous research, suggested abnormal mitochondrial function with decreased mitochondrial bioenergetics, altered mitochondrial structure and dynamics, and decreased mitochondrial complex activities in mice models of cardiac proteotoxicity (i.e., D7-DesTg and αB-Crystallin<sup>R120G</sup>) where all these changes were associated to intracardiac deposition of protein aggregates<sup>30,31</sup>. In addition, mitochondrial insufficiencies with decreased cytochrome oxidase, pyruvate dehydrogenase, and α-ketoglutarate dehydrogenase activities were associated with AD<sup>57</sup>. Several studies have found a link between mitochondrial function and AD phenotype. Using different in vivo models of AD, previous studies have undeniably exhibited mitochondrial dysfunction with impaired mitochondrial dynamics with decreased mitochondrial fusion and increased fission, decreased ER-mitochondria interaction, reduced respiration with decreased complex I activity in hippocampus (and its astrocytes), cerebral cortex, and total brain of APPSWE/ PS1 Tg mice, 3xTg AD mice, and P130L Tau Tg mice<sup>46,58-60</sup>. Studies employing in vitro models using APP overexpressing primary neurons, astrocytes, neuroblastoma cells (SH-SY5Y)<sup>61</sup>, and neuroblasts (M17 cells)<sup>47</sup> corroborated with the findings of in vivo models displaying decreased mitochondrial respiratory control ratio and ATP levels and altered mitochondrial morphology.

We also found altered mitochondrial supercomplex formation with Complex III and Complex IV degradation in APP<sup>SWE</sup>/PS1 Tg mice. Mitochondria participates in ATP production as a function of the electron transport chain (ETC) complexes, wherein the electron is transported from complexes I, II, and III to the electron recipient to produce NADH and FADH. The complexes in the ETC are known to combine at stoichiometric ratios and form different supercomplex (SCs) to facilitate electron transfer<sup>62,63</sup>. Studies have shown decreased SC formation in the cortex, primary neurons, and astrocytes from mice and rat models of aging and neurodegenerative diseases<sup>64,65</sup>. A $\beta$  accumulation has also shown altered SC formation, leading to mitochondrial dysfunction in APP C99 overexpressing cells and mice brains<sup>66</sup>. Our previous studies also demonstrated an overall decrease in SC and all the mitochondrial complexes due to mitochondrial accumulation of protein aggregates in  $\alpha$ B-Crystallin<sup>R120G</sup> mice<sup>31</sup>. Besides, SC stability is also perturbed by increased ROS<sup>62,63</sup>. Correlating with the mouse models of cardiac proteotoxicity, APP<sup>SWE</sup>/PS1 Tg hearts showed altered mitochondrial dynamics, reduced antioxidant protein levels, reduced mitochondrial respiration, and complex activities. Further studies are required to dissect whether mitochondrial dysfunction and altered mitochondrial dynamics are caused by increased oxidative stress or vice versa and their mechanism.

Mitochondrial protein clearance has been allied with protein aggregation and neurodegenerative diseases (including AD). Studies have indicated accelerated synthesis or impaired clearance of Aβ aggregates contributes to AD pathogenesis<sup>49-51</sup>. Therefore, we evaluated changes in proteins involved in protein clearance, including inter-mitochondrial membrane serine protease (HtrA2), heat shock cognate protein 70 (hsc70), mitochondrial matrix serine proteases (ClpP, LonP1, and paraplegin), stress-inducible heat shock protein 60 (HSP60), and inner mitochondrial membrane serine protease (Omal). APPSWE/PS1 Tg hearts exhibited decreased HtrA2, ClpP, LonP1, and HSP60 protein levels. Studies reported that A $\beta$  accumulation in AD and  $\alpha$ -synuclein accumulation in Parkinson's Disease (PD) directly impair LonP1 and ClpP protease activity, further causing mitochondrial dysfunction<sup>67,68</sup>. In addition, depletion of LonP1 and ClpP has been linked with abnormal protein aggregation. Studies also suggested the direct interaction of LonP1 with A $\beta$  aggregates in AD and has been shown to work in concert with HSP70 to activate unfolded protein response<sup>67,69</sup>. HSP60 primarily mediates protection against protein aggregation, where activation of HSP60 has been shown to alleviate protein degradation 70,71. While studies have exhibited increased HSP60 levels in AD patients' lymphocytes, some studies have also demonstrated decreased HSP60 levels in the hippocampus from AD brains 70,71. HSP60 also directly interacts with APP and facilitates its translocation to mitochondria<sup>72</sup>. While all these changes in the expression of cellular proteases are associated with Aβ accumulation, increased oxidative stress caused by mitochondrial dysfunction and aging also causes proteostasis loss, leading to escalated protein aggregation<sup>71,73</sup>. In addition to the proteases, we also investigated changes in SAM50 (involved in protein sorting before its translocation to mitochondria via TOM40)<sup>74</sup>. Our studies demonstrated impaired proteostasis with increased cardiac accumulation of Aß aggregates. This

observed loss of proteostasis can be due to mitochondrial dysfunction, increased oxidative stress, and aging, which feed-forward to increased  $A\beta$  aggregation.

Although our study showed the presence of the presence of full-length APP and APP-breakdown products, amyloid deposition, and toxic amyloid oligomers, which may contribute to cardiac dysfunction and pathological remodeling, we do not know the source of the amyloid oligomers. APP<sup>SWE</sup>/PS1 Tg mice are generated by expressing the mutations in APP and PS1 gene using mouse prion protein (PrP) promoter<sup>75</sup>. Previous studies have largely indicated PrP drives transgenes in the brain and heart<sup>76</sup>. However, later studies suggested its expression in multiple tissues, including lungs, kidney, gastrointestinal tract, muscle, mammary glands, and lymphoid cells<sup>77</sup>, suggesting that transgene expression and protein aggregation lead to organ dysfunction. Therefore, our future studies will explore the possible accumulation of amyloid oligomers in other organs beyond the brain. However, we cannot rule out that cardiac dysfunction observed in these mice may be due to the cumulative effect of another organ dysfunction. As our study showed the phenotypic characterization of the APP<sup>SWE</sup>/PS1 Tg mice hearts, temporal studies should be performed to delineate the onset of cardiac dysfunction and define the molecular mechanism.

Overall, we explored the cardiac phenotype of aged APPSWE/PS1 Tg mice and reported several intriguing findings, including cardiac diastolic dysfunction, decreased grip strength and exercise intolerance, myocardial histopathological remodeling (increased collagen content and myocardial cross-sectional area), altered mitochondrial dynamics, altered antioxidant system, reduced levels of mitochondrial proteases, decreased OXPHOS and PDH protein levels, decreased Complex I and III activities, and decreased mitochondrial respiration. Based on the published literature and our findings in this study, we anticipate that myocardial accumulation of  $A\beta$  protein aggregate drives all these pathological changes. We assume that  $A\beta$ -induced mitochondrial dysfunction leads to cardiac dysfunction in the APPSWE/PS1 Tg heart. However, further studies are required to pinpoint the mechanism of these  $A\beta$  accumulation-mediated pathological changes in the heart.

### Methods Animals

All methods in this study were reported in accordance with ARRIVE guidelines (https://arriveguidelines.org) for reporting animal experiments. APPSWE/PSEN1dE9 (APPSWE/PS1 Tg) (stock no: 034832-JAX) mice generated by coinjection of humanized constructs for human amyloid precursor protein Mo/HuAPP695swe) with Swedish mutations (K595N/M596L) and mutant human Presnelin 1 protein with exon-9-deleted variant (PSEN1dE9) was used to mimic the early-onset Alzheimer's disease in the experiments<sup>75,78</sup>. The mice were purchased from Jackson Laboratories (Bar Harbour, ME, USA) and were accommodated in an adequately controlled setting following 12 h light–dark cycle in well-maintained cages. The mice were provided with water and a regular chow diet ad libitum. They were cared for according to the guidelines mentioned in the Guide for the Care and Use of Laboratory Animals<sup>79</sup> and animal protocol approved by the Animal Care and Use Committee of LSU Health-Shreveport, following the NIH Guide for the Care and Use of Laboratory Animals. For all our experiments, we used an equal number of APPSWE/PS1 Tg transgenic mice and their littermate non-transgenic (Wt) control mice (male and female) at 24 months of age.

### Echocardiographic analysis

We used non-invasive transfhoracic longitudinal echocardiography in Wt and APPSWE/PS1 Tg mice to measure the cardiac function as previously described 30,31,80-83. Briefly, the mice were anesthetized using isoflurane, and echocardiography was performed with VisualSonics Vevo 3100 high-resolution micro-ultrasound imaging system (FUJIFILM, Toronto, ON, Canada) coupled with Vevo LAB 3.1.1 imaging software (https://www.visua lsonics.com/product/software/vevo-lab, VisualSonics, Toronto, ON, Canada)84 and the myocardial function parameters were measured using 40-MHz transducer. We used 2-dimensional M-mode measurements to assess the systolic parameters of cardiac function, including systolic and diastolic left ventricular (LV) volume (LV Vol;s and LV Vol;d, respectively), percent ejection fraction (%EF), systolic and diastolic LV internal diameter (LVID;s and LVID;d respectively), percent fractional shortening (%FS; calculated using the equation ((LVIDd-LVIDs)/ LVIDd × 100), Intraventricular septal thickness at diastole (IVS;d), Left ventricular posterior wall thickness at diastole (LVPW;d), and heart rate as beats per minute). Additionally, we used pulse-wave Doppler measurements of mitral inflow velocity to assess diastolic parameters of cardiac function, including transmitral flow velocity during early diastolic filling (E wave) and atrial contraction (A wave), early-to-late diastolic flow velocity (MV E/A) ratio, and contribution (in percentage) of atrial contraction to diastolic filling. We also used tissue Doppler measurement parameters, including early diastolic mitral annular velocity (E') at the septal wall and the relationship between early diastolic inflow and early diastolic tissue velocity (E/E') at the septal wall to assess the myocardial relaxation. Moreover, we also used speckle-tracking based analysis from B-mode echocardiography to measure reverse longitudinal and radial strain (global; measured as an average of six LV segments), and maximum time-to-peak delay (T2P<sub>Max</sub>), standard deviation (STD) of T2P and T2P/RR for longitudinal and radial strain to assess LV dyssynchrony and deformity.

### Grip strength

We measured the forelimb grip strength of Wt and APP<sup>SWE</sup>/PS1 Tg mice to assess skeletal muscle endurance capacity as described previously<sup>85–87</sup>. Briefly, the mice were acclimatized to the experimental room for at least 10 min before the experiment. After acclimation, we placed the mice on the mesh grid of the grip strength meter v1.0.6 (1027SM, https://www.colinst.com/products/grip-strength-meter, Columbus Instruments, Columbus, OH, USA). Then, the mouse tail was pulled away from the grip strength meter once they held the grid using their forelimbs. The gauge measured the maximum tension produced by the forelimbs at the time of release from the grid.

We allowed the mice to rest for 1 min following each measurement. Each mouse was subjected to this trial up to five times. We used the manufacturer's software for the grip strength meter to analyze the data for every trial.

### Exercise tolerance capacity

We used an exercise tolerance test to assess the exercise capacity of the skeletal muscles of Wt and APP<sup>SWE</sup>/PS1 Tg mice, as previously described<sup>86–88</sup>. Briefly, we subjected the mice to three training sessions to acclimatize mice to the treadmill (OxyletPro, Panlab; Harvard Apparatus, Holliston, MA, USA) followed by one week of rest time before the experiment for the mice. We acclimated the mice by placing them in a stationary but shockgrid (1.5 mA)-activated treadmill. The initial treadmill setting was at a walking speed of 6 m/min for 5 min, then gradually increasing the speed to 12 m/min for 12 min. Following rest time post-acclimation, the mice were subjected to an exercise tolerance test where the mice were placed on a shock grid-activated treadmill at 0<sup>0</sup> incline and allowed to run on the treadmill with gradually increasing speeds and inclinations until exhaustion<sup>86,88</sup>. Mice were categorized as exhausted if they spent more than 5 s on the shockgrid or got more than 10 shocks. We analyzed the data for exercise tolerance using Metabolism version 3.0 software (https://panlab.com/en/products/metabolism-software-panlab, Harvard Apparatus).

### Western blot

We used whole-cell fractions from hearts of Wt and APPSWE/PS1 Tg mice at 24 months of age to evaluate changes in different protein expressions. We prepared the total cellular fraction from the snap-frozen heart tissues using Cell Lytic M (Sigma-Aldrich, St. Louis, MO, USA) lysis buffer containing Complete Protease and Phosphatase Inhibitor Cocktail (Roche, Basel, Switzerland), as described previously 30,31,82. Briefly, we homogenized the heart tissue in the lysis buffer using a bead homogenizer. The tissue lysates were subsequently sonicated and centrifuged the homogenates at 12,000×g for 15 min to deposit insoluble cell debris. We used the soluble supernatant containing the whole protein for our further experiments. We measured the total protein content of the whole cell lysates using the modified Bradford reagent (Bio-Rad, Hercules, CA, USA) relative to a BSA standard curve (BioRad). We ran the samples through SDS-PAGE to separate the proteins using pre-cast 7.5% to 15% Criterion Gels (BioRad). We transferred the SDS-PAGE-subjected gels to polyvinylidene difluoride (PVDF) membranes (Bio-Rad). Subsequently, the transferred membranes were stained with PonceauS (Acros organics; 0.2% in 5% glacial acetic acid) to assess the total protein transferred on the membrane. Following PonceauS staining, we washed the membranes to clean the PonceauS, blocked (1 h with 5% non-fat dry milk), and incubated with primary antibodies (diluted in 1% BSA) overnight at 4 °C. Following primary antibody incubation, we washed the membranes with 1× wash buffer. Subsequently, we incubated them with alkaline phosphatase-conjugated secondary antibodies Jackson ImmunoResearch Laboratories, Inc., West Grove, PA, USA) (1:5000 in 5% nonfat dry milk). Finally, the membranes were developed using ECF reagent (Amersham, Amersham, UK), and imaged with Chemidoc Touch Imaging System (Bio-Rad). We then performed densitometric quantification for the protein level changes using ImageJ software version 1.53q (https://imagej.net/ij/, NIH, Bethesda, MD, USA). Data were normalized to TOM 20 and COX IV. The primary antibodies used in this manuscript are β-amyloid (1:1000; 803002; Biolegend), OXPHOS (1:1000; MS604; Abcam), PDH (1:1000; ab110406; Abcam), Catalase (1:500; 129805; Cell Signaling), Glutathione Peroxidase 1(GPX1; 1:500; ab108427; Abcam), SOD1 (1:500; 37385; Cell Signaling), MnSOD (1:500; 06984; Millipore), Drp1 (1:1000; 14647; Cell Signaling), pDrp-Ser616 (1:1000; 3455; Cell Signaling); pDrp-Ser637 (1:1000; 6319; Cell Signaling), Fis1 (1:200; sc-98900; Santa Cruz Biotechnology), OPA1 (1:1000; 80471; Cell Signaling), Mfn2 (1:1000; 9482; Cell Signaling), SAM50 (1:300; sc-100493; Santa Cruz Biotechnology), HtrA2 (1:500; AF1458; R&D Systems), HSC70 (1:1000; ab2788; Abcam), ClpP (1:200; sc-271284; Santa Cruz Biotechnology), LonP1 (1:1000; SAB1411647; Sigma), Hsp60 (1:300; sc-13115; Santa Cruz Biotechnology), Paraplegin (1:200; sc-514393; Santa Cruz Biotechnology), Oma1 (1:200; sc-515788; Santa Cruz Biotechnology), Tom 20 (1:200; sc-11415; Santa Cruz Biotechnology), pNF-κB (1:500; 3033; Cell Signaling), Total NF-κB (1:500; 4764; Cell Signaling), and MMP2 (1:1000; ab92536; Abcam), 8-OHdG (1:200; sc-139586; Santa Cruz Biotechnology), ATM (1:500; 2873; Cell Signaling), and ATR (1:500; 13934; Cell Signaling).

### Immunohistochemistry

We used immunohistochemistry on thin serial sections (5  $\mu$ m) of the heart tissue to observe the expression pattern of  $\beta$ -amyloid in Wt and APP<sup>SWE</sup>/PS1 Tg mice as described previously<sup>80</sup>. Briefly, we deparaffinized the paraffin-embedded tissues followed by sequential hydration, antigen retrieval with antigen unmasking solution (H-3300, Vector Laboratories, Burlingame, CA, USA). The antigen unmasked sections were subjected to blocking of endogenous peroxidases (0.3% v/v hydrogen peroxide; Bloxall, SP-6000, Vector Laboratories, Burlingame, CA, USA), and blocking with 5% serum (Vector Laboratories, Burlingame, CA, USA). Next, the blocked sections were exposed to the primary antibody (diluted at 1:100 in blocking serum) overnight at 4 °C in a humid chamber. Post-primary antibody incubation, the sections were washed with 1xPBS and incubated with secondary antibody (Vector Laboratories, Burlingame, CA, USA) for 1 h 30 min. The antigen–antibody interaction signal was enhanced using VECTASTAIN Elite ABC Peroxidase kit (PK-6100, Vector Laboratories, Burlingame, CA, USA). Following the staining of the heart sections, we subjected the sections to counterstaining with hematoxylin, dehydration, and mounting with Cytoseal XYL mounting medium (Thermo Scientific). The stained sections were then imaged using Olympus BX40 microscope (Olympus Life Science, Waltham, MA, USA) in brightfield mode. The primary antibody used in this manuscript is  $\beta$ -amyloid (1:100; 803002; Biolegend).

### **Immunofluorescence**

We used immunofluorescence staining on 5  $\mu$ m thin serial sections from the hearts of both Wt and APPSWE/PS1 Tg mice to examine the expression pattern of  $\beta$ -amyloid at the cellular level as described previously  $^{30,31}$ . The thin sections from paraffin-embedded tissue were sequentially deparaffinized, hydrated, antigen retrieved (by boiling at 100 °C in 10 mmol/L sodium citrate buffer (pH 6.0)), enhanced (using ITFX (Invitrogen)), and blocked (1 h at room temperature with 1% bovine serum albumin, 0.1% cold water fish skin gelatin, and 1% Tween 20 in PBS). Next, we incubated the blocked sections with primary antibodies (diluted in blocking buffer (1:100)) in a humid chamber, followed by Alexa Fluor conjugated respective secondary antibodies (1 h 30 min in a humid chamber) and DAPI (5 min). Next, we mounted DAPI-stained sections with Vectashield Hardset antifade mounting media (Vector Laboratories, Burlingame, CA, USA), and imaged them using a Nikon A1R high-resolution confocal microscope in an investigator-blinded manner. The primary and secondary antibodies we used were  $\beta$ -amyloid (1:100; 803002; Biolegend), Desmin (1:100; V1015; Biomeda), Anti-Oligomer A-11 (1:100; AHB0052; Life Technologies), Cardiac Troponin I (cTnI) (1:100; MAB1691; Millipore) Alexa Fluor 488 :(A11034; Invitrogen), and Alexa Fluor 568 (A11031; Invitrogen).

### Picro-Sirius Red (PSR) staining

Picro-Sirius Red staining was done on the 5 µm thin serial sections from the hearts of both Wt and APP<sup>SWE</sup>/PS1 Tg mice to evaluate the collagen deposition as an indicator of pathological remodeling of the heart using the previously described process<sup>30,81,82</sup>. Briefly, the thin serial sections were deparaffinized, hydrated, stained with Picro-Sirius Red (1 h at room temperature), and dehydrated. The stained sections were mounted with Cytoseal XYL mounting medium (Thermo Scientific) and imaged using an Olympus BX40 microscope (Olympus Life Science, Waltham, MA, USA) in brightfield mode. The heart images were then used to quantify collagen deposition. Using the ImageJ software version 1.53q (https://imagej.net/ij/, NIH, Bethesda, MD, USA), we determined collagen content in the heart as red-stained areas and non-stained cellular areas employing color-based thresholding. The collagen content was calculated as the percentage of red-stained area compared to the total surface area of each microscopic section from 10 to 12 high-magnification images that were investigator-blinded.

### Wheat Germ Agglutinin (WGA) staining

We used WGA staining to define the changes in cardiomyocytes' cross-sectional area (CSA) in Wt and APP/  $PS1^{SWE}$  Tg mice hearts as described previously  $^{30,81,82}$ . In summary, we used paraffin-embedded thin serial Sects. (5 µm) from the hearts of both groups. The myocardial sections were subjected to sequential deparaffinization, hydration, boiling mediated antigen retrieval (100 °C in 10 mmol/L sodium citrate buffer (pH 6.0)), and blocking (1% bovine serum albumin, 0.1% cold water fish skin gelatin, and 1% Tween 20 in PBS) followed by incubation with Alexa Fluor 488 conjugated Wheat Germ Agglutinin (WGA) (5 µg/mL; Invitrogen) and counterstaining of the nuclei with DAPI (Invitrogen). We mounted the stained sections with Vectashield Hardset antifade mounting media (Vector Laboratories). Post-staining, the slides were imaged using a Nikon A1R high-resolution confocal microscope (Nikon Instruments Inc. Melville, NY, USA) in an investigator-blinded manner, and the cardiomyocytes' CSA was measured using ImageJ software version 1.53q (https://imagej.net/ij/, NIH, Bethesda, MD, USA).

### Hematoxylin and Eosin (H&E) staining

We used H&E staining on 5  $\mu$ m thin serial sections from the hearts of both Wt and APP<sup>SWE</sup>/PS1 Tg mice to assess immune cell infiltration according to manufacturer's instructions (H&E staining kit; H3502; Vector Laboratories) and as described previously<sup>81,87</sup>. Subsequently, we mounted the stained sections using Cytoseal XYL mounting medium (Thermo Scientific) and imaged them using an Olympus BX40 microscope (Olympus Life Science, Waltham, MA, USA) in brightfield mode and a magnification of 20X.

### Mitochondrial isolation from the heart

We isolated mitochondrial fractions from the hearts of Wt and APP<sup>SWE</sup>/PS1 Tg mice, as described previously  $^{31,80,82}$ , to assess mitochondrial function and subjected it to several experiments. Briefly, we anesthetized the mice using isoflurane, excised the hearts, and isolated the ventricles, followed by homogenization with glass/Teflon Potter Elvehjem homogenizer in mannitol-sucrose-ethylene glycol tetraacetic acid (EGTA) buffer (225 nM mannitol, 75 mM sucrose, 5 mM HEPES, and 1 mM EGTA (pH7.4)). Using differential centrifugation at 600xg for 6 min and  $10,000\times g$  for 10 min, respectively, followed by wash steps, we obtained fresh mitochondrial fraction and used it for subsequent experiments.

### Non-gradient blue native polyacrylamide gel electrophoresis (BN-PAGE)

We used freshly isolated mitochondrial fractions to assess mitochondrial supercomplex dynamics, as described previously  $^{31,81,89-91}$ . Briefly, we used an extraction buffer containing 50 mM Bis-Tris (pH 7.0), 1% n-dodecyl- $\beta$ -d-maltoside (vol/vol), and 750 mM  $\epsilon$ -amino-N-caproic acid to resuspend isolated mitochondria followed by incubation on ice for 1 h. The mitochondrial suspension was then subsequently sonicated, centrifuged (8000×g for 10 min), and mixed with  $10\times BN$ -PAGE loading buffer containing 0.5 M  $\epsilon$ -amino-N-caproic acid and 3% Serva Blue G-250 (wt/vol). We loaded equal amounts of protein sample in 6% non-gradient polyacrylamide gels (made using gel buffer containing 500 mM aminocaproic acid and 50 mM Bis-Tris, pH 7.0) and resolved them at room temperature using cathode buffer (50 mM Tricine, 15 mM Bis-Tris, pH 7.0), 0.02% Serva blue G-250 (wt/vol), anode buffer (50 mM Bis-Tris pH 7.0). We ran the gels at 150 V until the front blue line reached two-thirds of the gel and then replaced the cathode buffer with the one without Serva blue G-250 (50 mM Tricine, 15 mM

Bis-Tris, pH 7.0) followed by the run at 250 V until the end. After the completion of the run, the gels were stained with Coomassie blue (Bio-Rad), imaged on ChemiDoc Touch Imaging System (Bio-Rad), transferred on PVDF membrane, and incubated with anti-OXPHOS (1:1000, ab110413, Abcam). The primary antibody-exposed membranes were developed using ECF substrates to detect and confirm the relative expression and localization of specific complexes' subunits.

### Complex activity assays

We used isolated mitochondrial fractions to analyze electron transport system complex-specific activities<sup>81,82,92</sup>. To measure complex-specific activity for all the complexes, we permeabilized the isolated mitochondrial fraction by subjecting it to three freeze-thaw cycles. Following permeabilization, for total complex I activity, we measured the NADH (10 µmol/L) oxidation-mediated absorbance changes at 340 nm for 2 min in an assay mixture with 2 µg mitochondrial protein in 50 mmol/L potassium phosphate buffer (pH 7.5), 1 mg/mL BSA, 250 µmol/L KCN, and 6 µL of ubiquinone1 (10 mM) in 1 mL cuvette using DS-11 FX+spectrophotometer (DeNovix, Wilmington, DE). The measurement was repeated in an assay mixture containing rotenone (complex I inhibitor), and specific complex I activity was calculated as rotenone-sensitive activity expressed as nanomoles/minute per milligram of mitochondrial protein. Secondly, we evaluated complex II activity by measuring reduction of 2,6-dichlorophenolindophenol coupled to complex II catalyzed reduction of decylubiquinone in an assay mixture containing 2 µg mitochondrial protein in 25 mmol/L potassium phosphate buffer (pH 7.5), 1 mg/mL BSA, and 20 mmol/L succinate (after incubation at 37 °C for 10 min) following measurement of 2,6-dichlorophenolindophenol (DCPIP; 80 μmol/L) reduction (600 nm for 3 min). We repeated this measurement in the presence of malonate (complex II inhibitor) and calculated the specific complex II activity as malonate-specific activity expressed as nanomoles/ minute per milligram of mitochondrial protein. Lastly, to measure complex III activity, we evaluated cytochrome C (75 µmol/L) reduction at 550 nm for 2 min in the reaction mixture containing 5 µg mitochondrial protein in 50 mmol/L potassium phosphate buffer (pH 7.5), 250 μmol/L KCN, 100 μmol/L EDTA, and 60 μmol/L decylubiquinol in the presence and absence of antimycinA1 (complex III inhibitor; 10 µmol/L). We then calculated specific complex III activity as antimycin A-sensitive activity expressed as nanomoles/minute per milligram of mitochondrial protein. Extinction coefficients used for the evaluation of complex I, II, and III activities are NADH (6.2 mM<sup>-1</sup> cm<sup>-1</sup>), DCPIP (19.1 mM<sup>-1</sup> cm<sup>-1</sup>), and reduced cytochrome C (18.5 mM<sup>-1</sup> cm<sup>-1</sup>), respectively.

### Mitochondrial bioenergetics

To assess the mitochondrial function in terms of its bioenergetics, we used freshly isolated mitochondrial fraction and subjected to seahorse in an XFe24 Extracellular Flux Analyzer (Seahorse Biosciences, North Billerica, MA) as described previously  $^{80,82,83}$ . Following isolation, mitochondrial isolates (50 µg/well) were seeded in XF24 culture plates and measured the respiration in mitochondrial assay buffer (220 mmol/L mannitol, 7 mmol/L sucrose, 10 mmol/L KH2PO4, 5 mmol/L MgCl2, 2 mmol/L HEPES, 1 mmol/L EGTA, 0.2% fatty acid–free bovine serum albumin, pH 7.4) at basal condition followed by sequential addition of 1 µg/mL oligomycin (ATP-synthase inhibitor), 4 µmol/L FCCP (a mitochondrial uncoupler), and 0.5 µmol/L rotenone (a complex I inhibitor) plus 0.5 µmol/L antimycin A (a complex III inhibitor) using Wave version 2.6.1.56 software (https://www.agilent.com/en/product/cell-analysis/real-time-cell-metabolic-analysis/xf-software/seahorse-wave-desktop-software-740897, North Billerica, MA). We presented the mitochondrial OCR values as pmol/min/µg protein.

### Statistical analysis

We used GraphPad Prism software v9.2.0 (https://www.graphpad.com/, La Jolla, CA, USA) to perform all the statistical analyses and expressed all the data as ± SEM. We tested all the data sets for normality using the Kolmogorov-Smirnov test. For the data set that passed the normality test, we used a two-tailed, unpaired Student's t-test, followed by Tukey's post hoc test, and the data sets that didn't pass the normality test were analyzed using Kruskal–Wallis test. We presented the analyzed data set in graphs showing the median and interquartile range as well as dots. Upon analysis, the *p* value of less than 0.05 was considered statistically significant. We performed all the studies in an investigator-blinded manner.

### Data availability

All the raw data for Western Blots generated and analyzed for this manuscript are included in this published article. All the other datasets used in this manuscript are available from the corresponding author upon request.

Received: 27 February 2024; Accepted: 15 July 2024

### Published online: 19 July 2024

### References

- 1. 12023 Alzheimer's disease facts and figures. Alzheimers Dement 19, 1598-1695 (2023). https://doi.org/10.1002/alz.13016
- Liu, P. P., Xie, Y., Meng, X. Y. & Kang, J. S. History and progress of hypotheses and clinical trials for Alzheimer's disease. Signal Transduct. Target Ther. 4, 29. https://doi.org/10.1038/s41392-019-0063-8 (2019).
- Yokoyama, M., Kobayashi, H., Tatsumi, L. & Tomita, T. Mouse models of Alzheimer's disease. Front. Mol. Neurosci. 15, 912995. https://doi.org/10.3389/fnmol.2022.912995 (2022).
- 4. Wang, D. K. et al. Mitochondrial dysfunction in oxidative stress-mediated intervertebral disc degeneration. Orthop. Surg. 14, 1569–1582. https://doi.org/10.1111/os.13302 (2022).
- 5. Takasugi, N. et al. The role of presenilin cofactors in the gamma-secretase complex. Nature 422, 438–441. https://doi.org/10.1038/nature01506 (2003).
- 6. Knopman, D. S. et al. Alzheimer disease. Nat. Rev. Dis. Primers 7, 33. https://doi.org/10.1038/s41572-021-00269-y (2021).

- 7. Di, J. et al. Abnormal tau induces cognitive impairment through two different mechanisms: synaptic dysfunction and neuronal loss. Sci. Rep. 6, 20833. https://doi.org/10.1038/srep20833 (2016).
- 8. Kikuchi, K., Kidana, K., Tatebe, T. & Tomita, T. Dysregulated metabolism of the amyloid-beta protein and therapeutic approaches in Alzheimer disease. *J. Cell Biochem.* 118, 4183–4190. https://doi.org/10.1002/jcb.26129 (2017).
- 9. Breijyeh, Z. & Karaman, R. Comprehensive review on Alzheimer's disease: Causes and treatment. Molecules 25, 5789 (2020).
- Drummond, E. & Wisniewski, T. Alzheimer's disease: experimental models and reality. Acta Neuropathol. 133, 155–175. https://doi.org/10.1007/s00401-016-1662-x (2017).
- 11. Jankowsky, J. L. & Zheng, H. Practical considerations for choosing a mouse model of Alzheimer's disease. *Mol. Neurodegener.* 12, 89. https://doi.org/10.1186/s13024-017-0231-7 (2017).
- 12. Sanchez-Varo, R. et al. Transgenic mouse models of Alzheimer's disease: An integrative analysis. Int. J. Mol. Sci. 23, 5404 (2022).
- Gotz, J., Bodea, L. G. & Goedert, M. Rodent models for Alzheimer disease. Nat. Rev. Neurosci. 19, 583–598. https://doi.org/10. 1038/s41583-018-0054-8 (2018).
- Jardanhazi-Kurutz, D. et al. Distinct adrenergic system changes and neuroinflammation in response to induced locus ceruleus degeneration in APP/PS1 transgenic mice. Neuroscience 176, 396–407. https://doi.org/10.1016/j.neuroscience.2010.11.052 (2011).
- 15. Knafo, S. et al. Morphological alterations to neurons of the amygdala and impaired fear conditioning in a transgenic mouse model of Alzheimer's disease. J. Pathol. 219, 41–51. https://doi.org/10.1002/path.2565 (2009).
- Tang, J. et al. Noggin and BMP4 co-modulate adult hippocampal neurogenesis in the APP(swe)/PS1(DeltaE9) transgenic mouse model of Alzheimer's disease. Biochem. Biophys. Res. Commun. 385, 341–345. https://doi.org/10.1016/j.bbrc.2009.05.067 (2009).
- 17. Spuch, C. et al. The effect of encapsulated VEGF-secreting cells on brain amyloid load and behavioral impairment in a mouse model of Alzheimer's disease. Biomaterials 31, 5608–5618. https://doi.org/10.1016/j.biomaterials.2010.03.042 (2010).
- Fernandez, A., Llacuna, L., Fernandez-Checa, J. C. & Colell, A. Mitochondrial cholesterol loading exacerbates amyloid beta peptide-induced inflammation and neurotoxicity. J. Neurosci. 29, 6394

  –6405. https://doi.org/10.1523/JNEUROSCI.4909

  –08.2009 (2009).
- Chen, L. et al. Studies on APP metabolism related to age-associated mitochondrial dysfunction in APP/PS1 transgenic mice. Aging (Albany NY) 11, 10242–10251. https://doi.org/10.18632/aging.102451 (2019).
- Stojakovic, A. et al. Partial inhibition of mitochondrial complex I ameliorates Alzheimer's disease pathology and cognition in APP/ PS1 female mice. Commun. Biol. 4, 61. https://doi.org/10.1038/s42003-020-01584-y (2021).
- 21. Misrani, A. et al. Mitochondrial deficits with neural and social damage in early-stage Alzheimer's disease model mice. Front. Aging Neurosci. 13, 748388. https://doi.org/10.3389/fnagi.2021.748388 (2021).
- 22. Gonzalez-Dominguez, R., Garcia-Barrera, T., Vitorica, J. & Gomez-Ariza, J. L. Region-specific metabolic alterations in the brain of the APP/PS1 transgenic mice of Alzheimer's disease. *Biochim Biophys. Acta* 1842, 2395–2402. https://doi.org/10.1016/j.bbadis. 2014.09.014 (2014).
- 23. Zheng, H. et al. The hypothalamus as the primary brain region of metabolic abnormalities in APP/PS1 transgenic mouse model of Alzheimer's disease. Biochim Biophys. Acta Mol. Basis Dis. 1864, 263–273. https://doi.org/10.1016/j.bbadis.2017.10.028 (2018).
- 24. An, L. et al. Cardiac dysfunction in a mouse vascular dementia model of bilateral common carotid artery stenosis. Front. Cardiovasc. Med. 8, 681572. https://doi.org/10.3389/fcvm.2021.681572 (2021).
- 25. Reed, A. L. et al. Diastolic dysfunction is associated with cardiac fibrosis in the senescence-accelerated mouse. Am. J. Physiol. Heart Circ. Physiol. 301, H824-831. https://doi.org/10.1152/ajpheart.00407.2010 (2011).
- de Lucia, C. et al. Echocardiographic strain analysis for the early detection of left ventricular systolic/diastolic dysfunction and dyssynchrony in a mouse model of physiological aging. J. Gerontol. A Biol. Sci. Med. Sci. 74, 455–461. https://doi.org/10.1093/ gerona/gly139 (2019).
- 27. Kittleson, M. M. et al. Cardiac amyloidosis: Evolving diagnosis and management: A scientific statement from the American Heart Association. Circulation 142, e7–e22. https://doi.org/10.1161/CIR.00000000000000092 (2020).
- 28. Griffin, J. M., Rosenblum, H. & Maurer, M. S. Pathophysiology and therapeutic approaches to cardiac amyloidosis. *Circ. Res.* 128, 1554–1575. https://doi.org/10.1161/CIRCRESAHA.121.318187 (2021).
- Rainer, P. P. et al. Desmin phosphorylation triggers preamyloid oligomers formation and myocyte dysfunction in acquired heart failure. Circ. Res. 122, e75–e83. https://doi.org/10.1161/CIRCRESAHA.117.312082 (2018).
- 30. Alam, S. et al. Aberrant mitochondrial fission is maladaptive in desmin mutation-induced cardiac proteotoxicity. J. Am. Heart Assoc. 7, e009289. https://doi.org/10.1161/JAHA.118.009289 (2018).
- 31. Alam, S. *et al.* Dysfunctional mitochondrial dynamic and oxidative phosphorylation precedes cardiac dysfunction in R120G-alphaB-crystallin-induced desmin-related cardiomyopathy. *J. Am. Heart Assoc.* **9**, e017195. https://doi.org/10.1161/JAHA.120.017195 (2020).
- 32. Giubilei, F. et al. Cardiac autonomic dysfunction in patients with Alzheimer disease: possible pathogenetic mechanisms. Alzheimer Dis. Assoc. Disord. 12, 356–361. https://doi.org/10.1097/00002093-199812000-00017 (1998).
- 33. Belohlavek, M. et al. Patients with Alzheimer disease have altered transmitral flow: echocardiographic analysis of the vortex formation time. J. Ultrasound Med. 28, 1493–1500. https://doi.org/10.7863/jum.2009.28.11.1493 (2009).
- Calik, A. N. et al. Altered diastolic function and aortic stiffness in Alzheimer's disease. Clin. Interv. Aging 9, 1115–1121. https://doi.org/10.2147/CIA.S63337 (2014).
- 35. Troncone, L. et al. Abeta amyloid pathology affects the hearts of patients with Alzheimer's disease: Mind the heart. J. Am. Coll. Cardiol. 68, 2395–2407. https://doi.org/10.1016/j.jacc.2016.08.073 (2016).
- 36. Sanna, G. D. et al. Cardiac abnormalities in Alzheimer disease: Clinical relevance beyond pathophysiological rationale and instrumental findings?. *JACC Heart Fail.* 7, 121–128. https://doi.org/10.1016/j.jchf.2018.10.022 (2019).
- Luciani, M. et al. Big tau aggregation disrupts microtubule tyrosination and causes myocardial diastolic dysfunction: from discovery to therapy. Eur. Heart J. 44, 1560–1570. https://doi.org/10.1093/eurheartj/ehad205 (2023).
- 38. Koike, M. A. *et al.* APP knockout mice experience acute mortality as the result of ischemia. *PLoS ONE* 7, e42665. https://doi.org/10.1371/journal.pone.0042665 (2012).
- Muller, U. C., Deller, T. & Korte, M. Not just amyloid: physiological functions of the amyloid precursor protein family. Nat. Rev. Neurosci. 18, 281–298. https://doi.org/10.1038/nrn.2017.29 (2017).
- Puig, K. L. & Combs, C. K. Expression and function of APP and its metabolites outside the central nervous system. *Exp. Gerontol.* 48, 608–611. https://doi.org/10.1016/j.exger.2012.07.009 (2013).
   Joachim, C. L., Mori, H. & Selkoe, D. J. Amyloid beta-protein deposition in tissues other than brain in Alzheimer's disease. *Nature*
- 41. Joachim, C. L., Mori, H. & Selkoe, D. J. Amyloid beta-protein deposition in tissues other than brain in Alzheimer's disease. *Nature* 341, 226–230. https://doi.org/10.1038/341226a0 (1989).
- 42. Pattison, J. S. et al. Cardiomyocyte expression of a polyglutamine preamyloid oligomer causes heart failure. Circulation 117, 2743–2751. https://doi.org/10.1161/CIRCULATIONAHA.107.750232 (2008).
- 43. Bonda, D. J., Wang, X., Perry, G., Smith, M. A. & Zhu, X. Mitochondrial dynamics in Alzheimer's disease: Opportunities for future treatment strategies. *Drugs Aging* 27, 181–192. https://doi.org/10.2165/11532140-00000000-00000 (2010).
- 44. Tonnies, E. & Trushina, E. Oxidative stress, synaptic dysfunction, and Alzheimer's disease. J. Alzheimers Dis. 57, 1105–1121. https://doi.org/10.3233/JAD-161088 (2017).
- 45. Manoharan, S. et al. The role of reactive oxygen species in the pathogenesis of Alzheimer's disease, Parkinson's disease, and huntington's disease: A mini review. Oxid. Med. Cell Longev. 2016, 8590578. https://doi.org/10.1155/2016/8590578 (2016).
- de la Cueva, M. et al. Amyloid-beta impairs mitochondrial dynamics and autophagy in Alzheimer's disease experimental models. Sci. Rep. 12, 10092. https://doi.org/10.1038/s41598-022-13683-3 (2022).

- 47. Wang, X. et al. Amyloid-beta overproduction causes abnormal mitochondrial dynamics via differential modulation of mitochondrial fission/fusion proteins. Proc. Natl. Acad. Sci. USA 105, 19318–19323. https://doi.org/10.1073/pnas.0804871105 (2008).
- 48. Flannery, P. J. & Trushina, E. Mitochondrial dynamics and transport in Alzheimer's disease. Mol. Cell. Neurosci. 98, 109–120. https://doi.org/10.1016/j.mcn.2019.06.009 (2019).
- Sweeney, P. et al. Protein misfolding in neurodegenerative diseases: implications and strategies. Transl. Neurodegener. 6, 6. https://doi.org/10.1186/s40035-017-0077-5 (2017).
- Sorrentino, V. et al. Enhancing mitochondrial proteostasis reduces amyloid-beta proteotoxicity. Nature 552, 187–193. https://doi. org/10.1038/nature25143 (2017).
- 51. Andrés-Benito, P. et al. Proteostatic modulation in brain aging without associated Alzheimer's disease-and age-related neuro-pathological changes. Aging 15, 3295–3330. https://doi.org/10.18632/aging.204698 (2023).
- 52. Jinawong, K., Apaijai, N., Chattipakorn, N. & Chattipakorn, S. C. Cognitive impairment in myocardial infarction and heart failure. Acta Physiol. (Oxf) 232, e13642. https://doi.org/10.1111/apha.13642 (2021).
- 53. Austin, B. P. et al. Effects of hypoperfusion in Alzheimer's disease. J. Alzheimers Dis. 26(Suppl 3), 123–133. https://doi.org/10.3233/IAD-2011-0010 (2011).
- 54. Gianni, D. et al. Protein aggregates and novel presenilin gene variants in idiopathic dilated cardiomyopathy. Circulation 121, 1216–1226. https://doi.org/10.1161/CIRCULATIONAHA.109.879510 (2010).
- 55. Caporizzo, M. A., Chen, C. Y., Bedi, K., Margulies, K. B. & Prosser, B. L. Microtubules increase diastolic stiffness in failing human cardiomyocytes and myocardium. *Circulation* 141, 902–915. https://doi.org/10.1161/CIRCULATIONAHA.119.043930 (2020).
- Murphy, J. et al. The cardiac dysfunction caused by metabolic alterations in Alzheimer's disease. Front. Cardiovasc. Med. 9, 850538. https://doi.org/10.3389/fcvm.2022.850538 (2022).
- 57. Gibson, G. E., Sheu, K. F. & Blass, J. P. Abnormalities of mitochondrial enzymes in Alzheimer disease. J. Neural. Transm. (Vienna) 105, 855–870. https://doi.org/10.1007/s007020050099 (1998).
- 58. Dematteis, G. et al. Proteomic analysis links alterations of bioenergetics, mitochondria-ER interactions and proteostasis in hip-pocampal astrocytes from 3xTg-AD mice. Cell Death Dis. 11, 645. https://doi.org/10.1038/s41419-020-02911-1 (2020).
- 59. David, D. C. et al. Proteomic and functional analyses reveal a mitochondrial dysfunction in P301L tau transgenic mice. J. Biol. Chem. 280, 23802–23814. https://doi.org/10.1074/jbc.M500356200 (2005).
- Castellani, R. et al. Role of mitochondrial dysfunction in Alzheimer's disease. J. Neurosci. Res. 70, 357–360. https://doi.org/10.1002/jnr.10389 (2002).
- Rhein, V. et al. Amyloid-beta leads to impaired cellular respiration, energy production and mitochondrial electron chain complex activities in human neuroblastoma cells. Cell Mol. Neurobiol. 29, 1063–1071. https://doi.org/10.1007/s10571-009-9398-y (2009).
- 52. Azuma, K., Ikeda, K. & Inoue, S. Functional mechanisms of mitochondrial respiratory chain supercomplex assembly factors and their involvement in muscle quality. *Int. J. Mol. Sci.* 21, 3182 (2020).
- 63. Novack, G. V., Galeano, P., Castano, E. M. & Morelli, L. Mitochondrial supercomplexes: Physiological organization and dysregulation in age-related neurodegenerative disorders. *Front. Endocrinol. (Lausanne)* 11, 600 (2020). https://doi.org/10.3389/fendo.2020.
- Frenzel, M., Rommelspacher, H., Sugawa, M. D. & Dencher, N. A. Ageing alters the supramolecular architecture of OxPhos complexes in rat brain cortex. Exp. Gerontol. 45, 563–572. https://doi.org/10.1016/j.exger.2010.02.003 (2010).
- 65. Lopez-Fabuel, I., Resch-Beusher, M., Carabias-Carrasco, M., Almeida, A. & Bolanos, J. P. Mitochondrial Complex I activity is conditioned by Supercomplex I-III(2-)IV assembly in brain cells: Relevance for Parkinson's disease. *Neurochem. Res.* 42, 1676–1682. https://doi.org/10.1007/s11064-017-2191-2 (2017).
- 66. Pera, M. et al. Increased localization of APP-C99 in mitochondria-associated ER membranes causes mitochondrial dysfunction in Alzheimer disease. EMBO J. 36, 3356–3371. https://doi.org/10.15252/embj.201796797 (2017).
- 67. Wang, W. et al. Intraneuronal beta-amyloid impaired mitochondrial proteostasis through the impact on LONP1. Proc. Natl. Acad. Sci. USA 120, e2316823120. https://doi.org/10.1073/pnas.2316823120 (2023).
- 68. Hu, D. et al. Alpha-synuclein suppresses mitochondrial protease ClpP to trigger mitochondrial oxidative damage and neurotoxicity. Acta Neuropathol. 137, 939–960. https://doi.org/10.1007/s00401-019-01993-2 (2019).
- Shin, C. S. et al. LONP1 and mtHSP70 cooperate to promote mitochondrial protein folding. Nat. Commun. 12, 265. https://doi. org/10.1038/s41467-020-20597-z (2021).
- 70. Zimbone, S., Di Rosa, M. C., Chiechio, S. & Giuffrida, M. L. Exploring the Role of Hsp60 in Alzheimer disease and Type 2 diabetes: Suggestion for common drug targeting. *Int. J. Mol. Sci.* 24, 12546 (2023).
- 71. Campanella, C. et al. Heat shock proteins in Alzheimer's disease: Role and targeting. Int. J. Mol. Sci. 19, 2603 (2018).
- 72. Walls, K. C. et al. Swedish Alzheimer mutation induces mitochondrial dysfunction mediated by HSP60 mislocalization of amyloid precursor protein (APP) and beta-amyloid. J. Biol. Chem. 287, 30317–30327. https://doi.org/10.1074/jbc.M112.365890 (2012).
- 73. Vilchez, D., Saez, I. & Dillin, A. The role of protein clearance mechanisms in organismal ageing and age-related diseases. *Nat. Commun.* 5, 5659. https://doi.org/10.1038/ncomms6659 (2014).
- 74. Kozjak, V. et al. An essential role of Sam50 in the protein sorting and assembly machinery of the mitochondrial outer membrane. J. Biol. Chem. 278, 48520–48523. https://doi.org/10.1074/jbc.C300442200 (2003).
- 75. Jankowsky, J. L. et al. Mutant presenilins specifically elevate the levels of the 42 residue beta-amyloid peptide in vivo: evidence for augmentation of a 42-specific gamma secretase. Hum. Mol. Genet. 13, 159–170. https://doi.org/10.1093/hmg/ddh019 (2004).
- 76. Borchelt, D. R. et al. A vector for expressing foreign genes in the brains and hearts of transgenic mice. Genet. Anal.: Biomol. Eng. 13, 159–163. https://doi.org/10.1016/S1050-3862(96)00167-2 (1996).
- 77. Zomosa-Signoret, V., Arnaud, J.-D., Fontes, P., Alvarez-Martinez, M.-T. & Liautard, J.-P. Physiological role of the cellular prion protein. Vet. Res. 39, 09 (2008).
- 78. Jankowsky, J. L. et al. Co-expression of multiple transgenes in mouse CNS: a comparison of strategies. Biomol. Eng. 17, 157–165. https://doi.org/10.1016/s1389-0344(01)00067-3 (2001).
- 79. Council, N. R., Studies, D. E. L., Research, I. L. A. & Animals, C. U. G. C. U. L. Guide for the Care and Use of Laboratory Animals: Eighth Edition. (National Academies Press, 2010).
- 80. Abdullah, C. S. *et al.* Methamphetamine induces cardiomyopathy by Sigmar1 inhibition-dependent impairment of mitochondrial dynamics and function. *Commun. Biol.* **3**, 682. https://doi.org/10.1038/s42003-020-01408-z (2020).
- 81. Abdullah, C. S. et al. Mitochondrial dysfunction and autophagy activation are associated with cardiomyopathy developed by extended methamphetamine self-administration in rats. Redox Biol. 58, 102523. https://doi.org/10.1016/j.redox.2022.102523 (2022).
- 82. Abdullah, C. S. et al. Cardiac dysfunction in the sigma 1 receptor knockout mouse associated with impaired mitochondrial dynamics and bioenergetics. J. Am. Heart Assoc. 7, e009775. https://doi.org/10.1161/JAHA.118.009775 (2018).
- 83. Abdullah, C. S. et al. Doxorubicin-induced cardiomyopathy associated with inhibition of autophagic degradation process and defects in mitochondrial respiration. Sci. Rep. 9, 2002. https://doi.org/10.1038/s41598-018-37862-3 (2019).
- 84. Rajan, K. B. et al. Population estimate of people with clinical Alzheimer's disease and mild cognitive impairment in the United States (2020–2060). Alzheimers Dement. 17, 1966–1975. https://doi.org/10.1002/alz.12362 (2021).
- 85. Takeshita, H. *et al.* Modified forelimb grip strength test detects aging associated physiological decline in skeletal muscle function in male mice. *Sci. Rep.* 7, 42323. https://doi.org/10.1038/srep42323 (2017).

- 86. Aishwarya, R. et al. Molecular characterization of skeletal muscle dysfunction in Sigma 1 receptor (Sigmar1) knockout mice. Am. J. Pathol. 192, 160–177. https://doi.org/10.1016/j.aipath.2021.10.003 (2022).
- 87. Aishwarya, R. et al. Pathological sequelae associated with skeletal muscle atrophy and histopathology in G93A\*SOD1 mice. Muscles 2, 51–74 (2023).
- 88. Petrosino, J. M. et al. Graded maximal exercise testing to assess mouse cardio-metabolic phenotypes. PLoS ONE 11, e0148010. https://doi.org/10.1371/journal.pone.0148010 (2016).
- 89. Jha, P., Wang, X. & Auwerx, J. Analysis of mitochondrial respiratory chain supercomplexes using blue native polyacrylamide gel electrophoresis (BN-PAGE). Curr. Protoc. Mouse Biol. 6, 1–14. https://doi.org/10.1002/9780470942390.mo150182 (2016).
- 90. Yan, L. J. & Forster, M. J. Resolving mitochondrial protein complexes using nongradient blue native polyacrylamide gel electro-phoresis. *Anal. Biochem.* 389, 143–149. https://doi.org/10.1016/j.ab.2009.03.043 (2009).
- 91. Luo, X., Wu, J., Jin, Z. & Yan, L. J. Non-gradient Blue Native polyacrylamide gel electrophoresis. *Curr. Protoc. Protein Sci.* 87, 11–29. https://doi.org/10.1002/cpps.21 (2017).
- 92. Spinazzi, M., Casarin, A., Pertegato, V., Salviati, L. & Angelini, C. Assessment of mitochondrial respiratory chain enzymatic activities on tissues and cultured cells. *Nat. Protoc.* 7, 1235–1246. https://doi.org/10.1038/nprot.2012.058 (2012).

### Acknowledgements

We would like to thank the Animal Models and Histology Core (RRID:SCR\_024776; https://coremarketplace.org/RRID:SCR\_024776), Redox Molecular Signaling Core (RRID:SCR\_024778; https://coremarketplace.org/RRID:SCR\_024778), CAIPP Bioinformatics and Modeling Core (RRID:SCR\_024779; https://coremarketplace.org/RRID:SCR\_024779), CAIPP Immunophenotyping Core (RRID:SCR\_024781; https://coremarketplace.org/RRID:SCR\_024781), Research Core Facility (RRID:SCR\_024775; https://coremarketplace.org/RRID:SCR\_024775), Small Animal Imaging Facility (RRID:SCR\_024777; https://coremarketplace.org/RRID:SCR\_024777) for technical support.

### **Author contributions**

R.A. and M.S.B. conceptualized the study; R.A. and M.S.B. designed the experiments; R.A., C.S.A., and N.S.R. performed all experiments and participated in analyses; M.A.N.B. performed statistical analysis; X.L., N.D., K.S., A.W.O., and C.G.K. contributed to analytic tools and contributed to reagents; R.A. and M.S.B. wrote the manuscript, and all of the authors have read, edited, and approved the paper.

### Funding

This work was supported by the National Institutes of Health grants: R01HL145753, R01HL145753-01S1, R01HL145753-03S1, and R01HL172970 to M.S.B.; NIH R01 HL098435, HL133497, and HL141155 to A.W.O; P20GM121307 and R01 HL149264 to C.G.K.; LSUHSC-S Malcolm Feist fellowship from the Center for Cardiovascular diseases and Sciences and AHA postdoctoral fellowship (20POST35210789) to C.S.A.; AHA predoctoral fellowship (24PRE1196230) and LSUHSC-S Malcolm Feist pre-doctoral fellowship from the Center for Cardiovascular diseases and Sciences to N.S.R.; AHA postdoctoral fellowship (23POST1027293) and LSUHSC-S Malcolm Feist postdoctoral fellowship from the Center for Cardiovascular diseases and Sciences to R.A.

### Competing interests

The authors declare no competing interests.

### Additional information

**Supplementary Information** The online version contains supplementary material available at https://doi.org/10.1038/s41598-024-67638-x.

Correspondence and requests for materials should be addressed to M.B.

Reprints and permissions information is available at www.nature.com/reprints.

**Publisher's note** Springer Nature remains neutral with regard to jurisdictional claims in published maps and institutional affiliations.

Open Access This article is licensed under a Creative Commons Attribution-NonCommercial-NoDerivatives 4.0 International License, which permits any non-commercial use, sharing, distribution and reproduction in any medium or format, as long as you give appropriate credit to the original author(s) and the source, provide a link to the Creative Commons licence, and indicate if you modified the licensed material. You do not have permission under this licence to share adapted material derived from this article or parts of it. The images or other third party material in this article are included in the article's Creative Commons licence, unless indicated otherwise in a credit line to the material. If material is not included in the article's Creative Commons licence and your intended use is not permitted by statutory regulation or exceeds the permitted use, you will need to obtain permission directly from the copyright holder. To view a copy of this licence, visit http://creativecommons.org/licenses/by-nc-nd/4.0/.

© The Author(s) 2024